

Regular Article

Low-Temperature controlled synthesis of nanocast mixed metal oxide spinels for enhanced OER activity



Patrick Guggenberger^{a,b}, Tatiana Priamushko^{a,c}, Prathamesh Patil^d, Justyna Florek^a, Daniel Garstenauer^{a,b}, Andreas Mautner^{e,1}, Jae Won Shin^f, Ryong Ryoo^g, Christian M. Pichler^{d,h}, Freddy Kleitz^{a,*}

^a Department of Functional Materials and Catalysis, University of Vienna, Währinger Straße 42, 1090 Vienna, Austria

^b Vienna Doctoral School in Chemistry (DoSChem), University of Vienna, Währinger Straße 42, 1090 Vienna, Austria

^c Forschungszentrum Jülich GmbH, Helmholtz Institute Erlangen-Nürnberg for Renewable Energy (IEK-11), Cauerstraße 1, 91058 Erlangen, Germany

^d CEST Centre of Electrochemical and Surface Technology, Viktor Kaplan-Straße 2, 2700 Wiener Neustadt, Austria

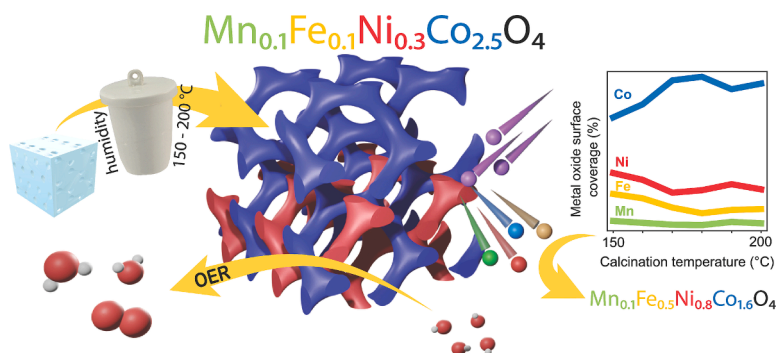
^e Department of Materials Chemistry, University of Vienna, Währinger Straße 42, 1090 Vienna, Austria

^f Center for Nanomaterials and Chemical Reactions, Institute for Basic Science (IBS), 291 Daehak-ro, Yuseong-gu, 34141 Daejeon, Republic of Korea

^g Department of Energy Engineering, Korea Institute of Energy Technology (KENTECH), Naju, 58330 Jeonnam, Republic of Korea

^h Institute of Applied Physics, Vienna University of Technology, Wiedner Hauptstraße 8-10, 1040 Vienna, Austria

GRAPHICAL ABSTRACT



ARTICLE INFO

Keywords:

Water electrolysis
Oxygen evolution reaction
Mixed metal oxides
Spinel
Nanocasting
Low-energy ion scattering
Electrochemical stability

ABSTRACT

The controlled cation substitution is an effective strategy for optimizing the density of states and enhancing the electrocatalytic activity of transition metal oxide catalysts for water splitting. However, achieving tailored mesoporosity while maintaining elemental homogeneity and phase purity remains a significant challenge, especially when aiming for complex multi-metal oxides. In this study, we utilized a one-step impregnation nanocasting method for synthesizing mesoporous Mn-, Fe-, and Ni-substituted cobalt spinel oxide ($\text{Mn}_{0.1}\text{Fe}_{0.1}\text{Ni}_{0.3}\text{Co}_{2.5}\text{O}_4$, MFNCO) and demonstrate the benefits of low-temperature calcination within a semi-sealed container at 150–200 °C. The comprehensive discussion of calcination temperature effects on porosity,

* Corresponding author.

E-mail address: freddy.kleitz@univie.ac.at (F. Kleitz).

¹ present address – Institute of Environmental Biotechnology, IFA-Tulln, University of Natural Resources and Life Sciences Vienna, Konrad-Lorenz-Straße 20, 3430 Tulln, Austria.

<https://doi.org/10.1016/j.jcis.2024.01.056>

Received 29 September 2023; Received in revised form 21 December 2023; Accepted 8 January 2024

Available online 11 January 2024

0021-9797/© 2024 The Author(s). Published by Elsevier Inc. This is an open access article under the CC BY license (<http://creativecommons.org/licenses/by/4.0/>).

particle size, surface chemistry and catalytic performance for the alkaline oxygen evolution reaction (OER) highlights the importance of humidity, which was modulated by a pre-drying step. The catalyst calcined at 170 °C exhibited the lowest overpotential (335 mV at 10 mA cm⁻²), highest current density (433 mA cm⁻² at 1.7 V vs. RHE, reversible hydrogen electrode) and further displayed excellent stability over 22 h (at 10 mA cm⁻²). Furthermore, we successfully adapted this method to utilize cheap, commercially available silica gel as a hard template, yielding comparable OER performance. Our results represent a significant progress in the cost-efficient large-scale preparation of complex multi-metal oxides for catalytic applications.

1. Introduction

Recent reports from the International Energy Agency (IEA) and the International Renewable Energy Agency (IRENA) emphasize the critical importance of reducing global greenhouse gas emissions quickly and efficiently to limit global warming to 1.5 °C. Renewable energy sources are key to achieving this goal, with hydrogen being one of the most promising energy carriers.[1,2] However, despite its potential as a clean and eco-friendly fuel and base chemical, 95 % of hydrogen production in 2020 (87 Mt) was generated through the CO₂-intensive steam reforming process, which is not sustainable. The IEA predicts that hydrogen demand will rapidly increase to 528 Mt in 2050. They also anticipate that until then, the share of environmentally friendly green hydrogen, generated by electrochemical water splitting using renewable energy sources, is expected to grow to 62 %.[1] To reach this goal, the efficiency of electrolyzers needs to be improved, specifically regarding the anodic oxygen evolution reaction (OER), which is sluggish due to a slow four-electron process. In addition, the state-of-the-art OER catalysts IrO₂ and RuO₂, which are currently considered the gold standard, have certain drawbacks such as being expensive, rare, and having limited durability under the demanding conditions required by practical electrolyzers.[3–7] To overcome these challenges, researchers have focused on studying non-noble first-row transition metal oxides, such as those based on Co, Ni, Fe, and Mn. These materials are abundant, affordable, and exhibit high stability for the alkaline OER.[8–11] Among them, the spinel cobaltites (Co₃O₄ and NiCo₂O₄) are especially versatile due to the ease of cation substitution with other first-row transition metals.[10,12–15] Such substitutions, for example with Ni, Fe, Mn, Zn, Li, Cu, V or W, can greatly improve the material's ability to catalyze the oxygen evolution reaction (OER) by changing the density of states, conductivity, and ad- and desorption free energies.[10,13,15–22] By introducing two or more substituting cations, even more flexibility is gained in the design of new electrocatalysts, allowing for further optimization of their performance.[20–24] Although such substitutions are a viable option, their complexity is often limited due to the challenges in synthesizing homogeneous, phase-pure mixed metal oxides through traditional methods such as sol-gel and co-precipitation. Besides the chemical composition, high specific surface area and good accessibility of the catalytically active sites are imperative for good heterogeneous catalysts.[11,25,26] Nanocasting, a well-established synthesis technique, produces ordered mesoporous transition metal oxides with high specific surface area and allows for precise control over pore size and geometry. This control can be achieved by using an appropriate ordered mesoporous silica template such as MCM-48, SBA-15, or KIT-6.[11,12,20,24,27] To synthesize multi-metal oxides using nanocasting, usually a high calcination temperature is required to obtain phase-pure materials.[20,28] Although promoting crystallinity, increased pore size, and phase purity, high calcination temperatures typically lead to decreased specific surface area (SSA) and worse mesoporous ordering, which results in overall poorer OER performance due to slower kinetics, higher overpotential, as charge transfer resistance.[20] To overcome this limitation, semi-sealed calcination containers can be used. These containers allow for the accumulation of humidity and NO_x gases during the decomposition of transition metal nitrate salts within silica pores. This leads to a reduction in calcination temperature, improves template replication, and provides some control over particle size.[29] In a previous study, we were able to

create well-ordered mesoporous mixed metal oxides at only 200 °C by using the container effect concept. By incorporating Fe and Mn cations into Ni_{0.5}Co_{2.5}O₄, we observed synergistic effects and obtained phase-pure catalysts with excellent OER performance. The Mn_{0.1}Fe_{0.1}Ni_{0.3}Co_{2.5}O₄ (MFNCO) catalyst exhibited lower overpotential, Tafel slope, and charge-transfer resistance compared to MFNCO calcined in an open container at 200 °C or 300 °C. We concluded that the difference in performance between the chemically indistinguishable samples was due to the mesostructure, which was influenced by the calcination conditions.[23] However, no detailed investigation regarding calcination conditions was performed and we anticipate, that there is much room for further improvement by fine-tuning of synthesis parameters, leading to more active, stable and economic catalysts. Therefore, our current study aims to elaborate appropriate conditions for the synthesis of mesoporous mixed metal oxide electrocatalysts by optimizing the semi-sealed low-temperature calcination approach. Using MFNCO as a model for complex mixed metal oxides, we screened calcination temperatures ranging from 150 – 200 °C and conducted extensive materials analysis to study the resulting surface characteristics and OER performance. By comparison of pre-drying temperatures, we assessed the influence of humidity during calcination. Additionally, we utilized high surface-sensitive low energy ion scattering spectroscopy (LEIS), to determine how the calcination temperatures impacted the mixed metal oxide's surface composition. To the best of our knowledge, this is the first time LEIS was applied to study nanocast materials. We used inductively coupled plasma mass spectrometry (ICP-MS) to evaluate the nanocast catalyst's electrochemical stability and potential dissolution during chronopotentiometry. Finally, we investigated the possibility of preparing these complex multi-metal oxides using a cheaper template to render the overall preparation more economical. In this regard, soft-templated synthesis approaches are sometimes favored due to their use of comparably cheap and commercially available pore-generating agents in the form of block-copolymers or surfactants. Although there are some inherent advantages with the direct soft-templating strategies, calcination temperatures above 350 °C, that are typically applied to achieve complete removal of the organic template, may also limit greatly the flexibility in terms of thermal treatment conditions for a controlled framework crystallization process at low-temperature.[30–33] Therefore, the synthesis procedure was successfully applied to a low-cost commercial silica gel as a hard template. This resulted in a significant cost reduction for producing mixed metal oxide catalysts through nanocasting, while retaining excellent electrocatalytic activity.

2. Experimental section

2.1. Reagents and materials

Pluronic P123, EO₂₀PO₇₀EO₂₀ (Sigma-Aldrich, Germany), HCl (37 %, Sigma-Aldrich, Germany), *n*-butanol (99 %, Thermo Fisher Scientific, Germany), tetraethyl orthosilicate (TEOS, 98 %, Thermo Fisher Scientific, Germany), ethanol (96 %, Brenntag, Austria), Co(NO₃)₂ · 6 H₂O (98.0–102.0 %, Thermo Fisher Scientific, Germany), Mn(NO₃)₂ · 6 H₂O (98+ %, Thermo Fisher Scientific, Germany), Ni(NO₃)₂ · 6 H₂O, 98 % (Thermo Fisher Scientific, Germany), Fe(NO₃)₃ · 9 H₂O (98+ %, metals basis, Thermo Fisher Scientific, Germany), *n*-hexane (≥99 %, Sigma-Aldrich, Germany), NaOH pellets (≥98 %, puriss. p.a., ACS reagent,

Sigma-Aldrich, Germany), Nafion®-117, (around 5 % in a mixture of water and lower aliphatic alcohols, Sigma-Aldrich, Germany), KOH pellets (85 %, VWR Chemicals, Germany), 2-propanol (≥ 99.8 % (GC), puriss. p.a., ACS reagent, Sigma-Aldrich, Germany), Al_2O_3 suspension (1 and 0.05 μm , MicroPolish suspension, Buehler Ltd., Germany), Rhodium internal standard (1000 mg L^{-1} $(\text{NH}_4)_2\text{RhCl}_3$, 5 % HCl, Labkings, Netherlands), Multi element standard solution (#23, Sb, As, Be, Cd, Ca, Cr, Co, Cu, Fe, Pb, Li, Mg, Mn, Mo, Ni, P, Se, Sr, Tl, Sn, Ti, V, Zn, 100 $\mu\text{g mL}^{-1}$ each in 5 % HNO_3 + Tr HF, LabKings, Netherlands), HNO_3 (69 %, ROTIPURAN® Supra, Roth, Germany) and Toray Carbon Paper (TGP-H-60, Thermo Fisher Scientific, Germany) were used as purchased.

2.2. Synthesis of ordered mesoporous silica

The KIT-6 silica template aged at 40 °C (denoted as KIT-6–40) exhibiting 3-D cubic *la3d* ordered mesoporous structure was synthesized according to the procedure described by Kleitz *et al.* [34] Briefly, Pluronic P123 (5.13 g) triblock-copolymer, which is acting as a structure-directing agent, was weighted into a 250 mL PP-bottle and completely dissolved in a mixture of concentrated HCl (9.92 g, 37 %) and distilled water (185.33 g) by stirring in an incubator overnight at 35 °C. The next day, *n*-butanol (5.13 g) was added as a co-surfactant. After another hour of stirring, TEOS was added at once and the mixture was continuously stirred at 35 °C for 24 h. Aging of the silica product was performed under static conditions at 40 °C for 48 h in a convection oven. The precipitate was isolated by filtration and dried first at 100 °C for 2 h and then at 140 °C overnight. Template removal was performed by suspending the white powder in a mixture of 200 mL of ethanol and two drops of concentrated HCl (37 %). The solvent was removed by filtration and the silica material was dried in an air atmosphere for two hours and calcined in a muffle oven in air at 550 °C for 3 h.

2.3. Synthesis of ordered mesoporous MFNCO using KIT-6–40 as a hard template

The one-step impregnation nanocasting synthesis was adapted from our previous work [23] Briefly, multimetallic oxides of the stoichiometric composition $\text{Mn}_{0.1}\text{Fe}_{0.1}\text{Ni}_{0.3}\text{Co}_{2.5}\text{O}_4$ were obtained by mixing a total amount of 1.75 g of transition metal nitrate salts (1.442 g / 4.9 mmol $\text{Co}(\text{NO}_3)_2 \cdot 6 \text{H}_2\text{O}$, 0.166 g / 0.6 mmol $\text{Ni}(\text{NO}_3)_2 \cdot 6 \text{H}_2\text{O}$, 0.080 g / 0.2 mmol $\text{Fe}(\text{NO}_3)_3 \cdot 9 \text{H}_2\text{O}$, and 0.058 g / 0.2 mmol $\text{Mn}(\text{NO}_3)_2 \cdot 6 \text{H}_2\text{O}$) with 1.0 g of KIT-6–40 (vacuum dried at 150 °C overnight) and 10 mL of *n*-hexane. The suspension was ground using an agate mortar until the solvent was evaporated. Subsequently, the powdery mixture was transferred into a 50 mL round bottom glass flask, *n*-hexane (30 mL) was added, and the suspension was refluxed under constant vigorous stirring at 80 °C overnight. The impregnated powders were obtained by filtration using a Büchner funnel and dried at room temperature (22 °C) overnight or in a convection oven at 70 °C for 4 h. After the drying step, 0.8 – 1.0 g of the transition metal nitrate salt-impregnated KIT-6 were weighted into ceramic calcination crucibles (LLG-Porcelain crucible tall, 15 mL outer diameter 30 mm, height 38 mm), which were equipped with a porcelain lid and thus served as semi-sealed containers for calcination in air atmosphere. The calcination was performed in a muffle oven (Nabertherm, model L9/11/C450, Germany) employing a heating rate of 1 °C min^{-1} and maintaining the indicated temperature (150, 160, 170, 180, 190, or 200 °C) for 6 h. The sample notation follows the (drying temperature/calcination temperature) scheme accordingly (e.g., 22/170). Removal of the KIT-6–40 silica template was achieved by two subsequent treatments with 30 mL of 2 M NaOH at 80 °C for 24 h, followed by two deionized water and one ethanol washing step. The black powders were air-dried at 70 °C overnight.

2.4. Synthesis of mesoporous MFNCO using commercial silica gel as a hard template

Following the nanocasting procedure described above, a commercial silica gel with broader pore size distribution and absence of mesopore ordering, but comparable pore size range, pore volume, and BET specific surface area was used as a cheap alternative to the KIT-6 template (Fig. S1.; Tab. S1). 2.44 g of transition metal nitrate salts (2.008 g / 6.9 mmol $\text{Co}(\text{NO}_3)_2 \cdot 6 \text{H}_2\text{O}$, 0.2408 g / 0.8 mmol $\text{Ni}(\text{NO}_3)_2 \cdot 6 \text{H}_2\text{O}$, 0.1115 g / 0.3 mmol $\text{Fe}(\text{NO}_3)_3 \cdot 9 \text{H}_2\text{O}$, and 0.0792 g / 0.3 mmol $\text{Mn}(\text{NO}_3)_2 \cdot 6 \text{H}_2\text{O}$) were mixed with 1.5 g of silica gel. After the impregnation, the batches were isolated by filtration and then split into two 1.9 g fractions which were calcined in separate crucibles. One synthesis batch was dried at 70 °C for 4 h and calcined in a semi-sealed crucible at 200 °C for 6 h (sample denoted as 70/200 SG) and another one, based on the synthesis conditions of the most active MFNCO OER catalyst from KIT-6, dried at 22 °C overnight and calcined in a semi-sealed crucible at 170 °C for 6 h (sample denoted as 22/170 SG). The silica template was removed by agitating the powders twice in 2 M NaOH at 80 °C for one day, followed by washing twice with deionized water and once with ethanol and then drying overnight at 70 °C.

2.5. Materials characterization

A Netzsch STA 449 F3 Jupiter (Selb, Germany) was employed to perform thermogravimetric analysis coupled with differential thermal analysis (TGA/DTA). The decomposition and conversion of transition metal nitrates impregnated into MFNCO within the pore framework of KIT-6–40 silica (after drying at 70 °C for at least 4 h) was measured using an Al_2O_3 crucible equipped with an Al_2O_3 lid (small pinhole in the middle) and were conducted from 25 °C to 600 °C, including a 30 min isothermal segment, in a constant synthetic air flow (20 mL min^{-1} ; 20 % O_2 , 80 % N_2) and a heating rate of 10 °C min^{-1} . The isothermal segments, which were set at 170, 180, and 190 °C, respectively, were used to acquire information on the decomposition of the nitrate salts in the semi-sealed container.

Nitrogen adsorption–desorption isotherms were recorded at – 196 °C using an Anton Paar QuantaTech Inc. iQ3 instrument (Boynton Beach, FL, USA). Outgassing was performed at 80 °C for 12 h. Data evaluation was conducted using the Anton Paar QuantaTech Inc. ASiQWin 5.2 software. The Brunauer-Emmet-Teller (BET) equation was applied to calculate the specific surface area (SSA) in the relative pressure range of 0.05 – 0.25 P/P_0 . To calculate the pore size distribution, the non-local density functional theory (NLDFT) kernel for oxide surfaces and cylindrical pore geometry was applied to the (metastable) adsorption branch of the isotherm in line with previous reports on similar oxide materials [12,20,27] (in the absence of pore blocking/cavitation effects on the hysteresis loop at P/P_0 around 0.45, using the desorption branch essentially leads to similar pore size distribution). Based on the Gurvich rule, the total pore volume was evaluated at the plateau region of the isotherm at $P/P_0 = 0.975$. [35]

Dynamic light scattering (DLS) measurements were conducted in triplicates with a Malvern DTS Nano Zetasizer. Before the measurements, the samples were suspended in deionized nanopure water (0.5 mg mL^{-1}) using an ultrasonic bath. The intensity particle size distribution was used for particle size analysis.

A PANalytical EMPYREAN equipped with a PIXcel^{3D} detector (Malvern PANalytical, United Kingdom) was used to record low- (LA-PXRD) and wide-angle powder X-ray diffractograms (WA-PXRD) with $\text{Cu K}_{\alpha 1+2}$ radiation generated at a voltage of 45 kV and a tube current of 40 mA. A Bragg-Brentano HD reflection geometry or a Focusing Mirror geometry setup was mounted for the WA-PXRD and LA-PXRD, respectively. The data was recorded in the continuous mode, employing a step size 2-theta of 0.013°. For the reflection and transmission measurements, data acquisition times per step were set at 150 s and 50 s, respectively. For the determination and refinement of crystal structures, a Bruker D8

ADVANCE powder diffractometer was operated in Bragg-Brentano pseudo focusing mode with theta/2-theta geometry. A zero-background silicon single-crystal sample holder was covered with a thin layer of grease to fix the powder. A one-dimensional silicon strip detector (Lynxeye) was used for all measurements. Every powder was measured in the 13° to 120° 2-theta range for three hours with an acceleration voltage of 40 kV and a beam current of 40 mA. Qualitative phase identification as well as Rietveld refinements were accomplished using the Topas 4.2 software.

Small Angle X-Ray Scattering (SAXS) measurements were performed using a Nano-inXider (Xenocs, France) with a $\text{Cu K}\alpha$ radiation source ($\lambda = 0.154$ nm). Data acquisition was performed at medium resolution mode and an exposure time of 600 s. The measurements were repeated 10 times and averaged using the XSACT (X-ray Scattering Analysis and Calculation Tool) software.

Scanning electron microscopic (SEM) images were taken using a Verios 460 field emission scanning electron microscope (FEI) at an accelerating voltage of 5 kV and a decelerating voltage of 4 kV, to have a landing voltage of 1 kV. The sample for SEM imaging was dispersed on carbon tape and kept under vacuum for 1 h before the imaging. Transmission electron microscopic (TEM) images were obtained using a Titan G2 ETEM (FEI) at an accelerating voltage of 300 kV. The sample for TEM imaging was prepared by dropping a small amount of ethanol containing a suspended powder sample on a holey carbon film-coated 300 mesh copper grid.

Surface characterization was performed using X-ray photoelectron spectroscopy (XPS, Nexsa, Thermo-Scientific, Massachusetts, USA) employing an Al-K α radiation source operating at 72 W and an integrated flood gun. The survey spectra were recorded with a pass energy of 200 eV, using the “Standard Lens Mode”, and CAE Analyzer Mode, and an energy step size of 1 eV. The diameter of the X-ray beam was 400 μm . High-resolution spectra of C 1 s, O 1 s, Co 2p, Ni 2p, Mn 2p, and Fe 2p were acquired with 50 passes at a pass energy of 50 eV and an energy step size of 0.1 eV. The XPS analysis was performed on the Avantage software (Thermo Avantage v5.9922), where the binding energy was calibrated using the C 1 s peak (284.8 eV).

A WITec alpha 300A equipped with a $100\times$ objective, a grating of 1200 g cm^{-1} , and a 531 nm laser with a beam power of 2 mW was used to record the Raman spectra. 40 measurements were accumulated with an acquisition time of 5 s each.

Low energy ion scattering (LEIS) measurements were performed on pressed powder samples using a Ne^+ primary ion beam accelerated at 5 keV. For each sample 15 spectra were recorded in the energy range 1000 – 1500 eV, analyzing two spots of 2.5×2.5 mm. Ar^+ sputtering (500 eV for 25 s) was applied in between measurements. Charge compensation was turned on to avoid charging effects. Reference measurements of pure nanocast single metal oxide powders with identical surface morphology were acquired and used for data evaluation. The evaluation was performed using the SurfaceLab 7.x software to fit the sample measurements with the reference measurement data and converted into oxide surface coverage (at%). The elemental ratios were derived from the respective stoichiometry of the oxides and their relative ratios.

For the determination of Fe content in the plain 1 M KOH electrolyte and the quantification of dissolved metal species (Mn, Fe, Ni, and Co) during the OER stability tests, inductively coupled plasma mass spectrometry (ICP-MS) was performed on an Agilent 7800 ICP-MS (Agilent Technologies, Tokyo, Japan). The instrument was equipped with an Agilent SPS 4 autosampler (Agilent Technologies, Tokyo, Japan), and the samples were analyzed in the gas flow mode (4 mL min^{-1}) and operated in He collision mode. For the quantification of Fe in the plain 1 M KOH electrolyte, a seven-point calibration was performed, using ^{103}Rh as internal standard and a multi-element standard with given concentrations of ^{55}Mn , ^{56}Fe , ^{59}Co , and ^{60}Ni . For the stability tests, a six-point calibration curve was obtained using the same internal and multi-element standards, but also an aliquot of 1 M KOH, matching the volume of electrolyte sampling, to compensate for the electrolyte contribution.

The samples were prepared by mixing 1 mL of sampled electrolyte with 1 mL of internal standard and 8 mL of 3 wt% HNO_3 solution. The sampled electrolyte volume was always replaced by fresh 1 M KOH electrolyte and the resulting dilution factor was taken into account during the evaluation.

2.6. Electrochemical OER measurements in three electrode RDE setup

The electrocatalysts were benchmarked for the OER utilizing a PGSTAT302N Autolab electrochemical workstation (Metrohm), using a glassy carbon rotating disc electrode (GC-RDE, 5 mm in diameter / geometric area of 0.196 cm^2 , Metrohm) as a working electrode, a graphite rod as a counter electrode, and a HydroFlex reversible hydrogen electrode (RHE, Gaskatel) as a reference electrode. The measurements were conducted in a three-electrode cell which was filled with 200 mL of 1.0 M KOH (VWR pellets dissolved in deionized pure water ($18.2\text{ M}\Omega\cdot\text{cm}$), 69.4 ppb Fe determined by ICP-MS, Tab. S2). 30 min prior and during the measurements, the cell was purged with N_2 gas, and a thermostat connected to the three-electrode cell's water jacket was used to maintain the temperature at 25°C . Before the measurements, the GC-RDE was polished on the polishing cloth with Al_2O_3 suspension (1 and 0.05 μm , Buehler Ltd) to give a mirror finish, followed by sonication in deionized pure water ($18.2\text{ M}\Omega\cdot\text{cm}$) for 5 min. The catalyst ink was prepared by suspending 4.8 mg of the catalyst in a mixture of 0.75 mL of $18.2\text{ M}\Omega\cdot\text{cm}$ deionized water, 0.25 mL of 2-propanol, and 50 μL of Nafion®-117 solution. A homogeneous ink was obtained after 30 min of sonication. 5.25 μL of the freshly prepared catalyst ink were dropped onto the GC-RDE (yielding a catalyst loading of 0.12 mg cm^{-2}) with an Eppendorf micropipette and dried under light irradiation. To ensure reproducibility, the measurements were repeated in triplicates. During the measurements, the RDE was rotated at 2000 RPM. For the cyclic voltammetry (CV) and linear sweep voltammetry (LSV) measurements, 90 % of the $i\text{R}$ -drop was corrected using the potentiostat software (Nova 2.1.5, Metrohm). First, three cycles of cyclic voltammetry were recorded with a sweep rate of 50 mV s^{-1} in a potential range between 0.7 V and 1.6 V vs. RHE. Then, three consecutive LSV curves were recorded with a scanning rate of 10 mV s^{-1} in anodic direction starting at 0.7 V up to a final potential of 1.7 V vs. RHE. The third LSV curve was used for data evaluation. The catalysts' reaction kinetics were further characterized by performing potentiostatic electrochemical impedance spectroscopy (EIS) measurements in the range from 100 kHz to 100 mHz and an amplitude of 5 mV at an applied potential of 1.6 V vs. RHE. To assess the electrochemical active surface area (ECSA), cyclic voltammograms were recorded with ascending scan rates (20 to 180 mV s^{-1} , 5 cycles per scan speed) in the non-Faradaic current region (1.0 – 1.1 V vs. RHE). By plotting the difference between anodic and cathodic capacitive current ($\Delta j = j_{\text{anode}} - j_{\text{cathode}}$) at 1.05 V vs. RHE at the respective scan rates against the applied scan rate, a linear plot was obtained. The double-layer capacitance (C_{dl}) was obtained by halving the slope of this plot. [36] The reference value of 0.04 mF cm^{-2} , which was reported to be a suitable approximation for oxidic OER catalysts in 1 M KOH, was used to estimate the ECSA. [20,37,38]

For the stability measurements of the 22/170 and 70/200 MFNCO samples, Toray carbon paper (TGP-H-60) was coated with catalyst ink via drop casting and dried at room temperature. The MFNCO loading on the carbon paper electrode was 0.5 mg cm^{-2} . Chronopotentiometry was performed for 22 h, applying a constant anodic current density of 10 mA cm^{-2} . During the OER stability measurements, electrolyte sample aliquots were collected in regular intervals to monitor the dissolution of metal species in the 1 M KOH electrolyte with ICP-MS. Before and after the stability tests, the catalyst-coated carbon paper was characterized with WA-PXRD and XPS to monitor changes to the bulk and surface chemistry of the catalysts.

3. Results and discussion

3.1. Thermal analysis

The thermal decomposition of the mixture of transition metal nitrate salts impregnated into KIT-6 silica was investigated by thermogravimetric analysis coupled with differential thermal analysis (TGA/DTA). For this purpose, an Al_2O_3 crucible with a lid was used to simulate semi-sealed calcination conditions. As depicted in Figure S2, three separate measurements with 30 min isothermal temperature (T_i) segments at 190, 180, and 170 °C were performed to investigate the decomposition behavior. The weight loss/transition metal salt decomposition in the first segment of the measurement up to the respective T_i was affected by increasing T_i (Tab. S3). The decomposition during the isothermal step was significantly influenced by T_i , indicating much slower decomposition kinetics at lower temperatures. At T_i of 170 °C and 180 °C, the conversion into MFNCO was not completed and was still progressing at a slow rate at the end of the isothermal segment (30 min), as displayed by the continuous weight loss throughout the isothermal segment and abrupt weight loss in the first minutes of the final segment. These results indicate that at roughly 190 °C, a tipping point is reached, where the dehydration/decomposition becomes a fast process. It should be noted that this small-scale TGA study does not directly translate to our actual synthesis conditions. However, it indicates a clear delay in the salt conversion rate at temperatures of 180 °C and below, hinting at an extended timeframe for the rearrangement of highly mobile molten precursors and intermediate salt species within the silica pore network.

3.2. Elemental composition, material structure and particle size

The elemental composition of the MFNCO materials synthesized via one-step impregnation nanocasting approach was analyzed using X-ray

fluorescence spectroscopy (XRF). The results summarized in Table S4 indicate a very low residual SiO_2 amount ($\text{Si} < 1$ at%), good match between targeted and achieved composition, and consistent metal ratios across the various MFNCO catalysts.

LA-PXRD and SAXS measurements (Fig. 1) revealed distinct mesopore ordering evidenced by 211 and 220 diffraction peaks, which can be correlated to the inverse replication of the initial 3-D cubic $la3d$ symmetry of the parent KIT-6 gyroid framework. The observed 110 reflection results from lower symmetry due to the use of KIT-6-40 as a template. KIT-6-40 exhibits two isolated pore-frameworks, which may lead to either shifted oxide subframeworks (as it was observed for some ordered mesoporous carbon materials) or domains of single subframework due to heterogeneous filling.[39–41] The SAXS measurements serve as a complementary technique, which offers a higher diffraction peak resolution. With both techniques, the materials that were pre-dried at 22 °C overnight and subsequently calcined at 150–180 °C for 6 h (22/150, 22/160, 22/170, and 22/180) as well as for the samples which were pre-dried at 70 °C and calcined at 190 and 200 °C (70/190, 70/200; Fig. 1a, b) showed well-resolved diffraction peaks. In contrast, the batches that were pre-dried at 22 °C overnight but calcined at higher temperatures (22/190 and 22/200), as well as the samples pre-dried at 70 °C and calcined below 190 °C (70/180, 70/170, 70/160) all exhibited clearly decreased peak intensities (Fig. 1c, d). This may arise due to smaller coherent scattering domain sizes in these samples. However, in the following sections covering transmission electron microscopy (TEM), high-resolution scanning electron microscopy (HR-SEM), and N_2 physisorption, we could demonstrate, that it reflects a decrease in mesopore ordering and an increase in irregularity within the KIT-6 replicated transition metal oxide (TMO) framework. Due to the appearance of two clearly distinguishable families of samples, we categorized the MFNCO samples into *ordered* (22/150, 22/160, 22/170, 22/180, 70/190, and 70/200) and *semi-ordered* samples (70/160, 70/170,

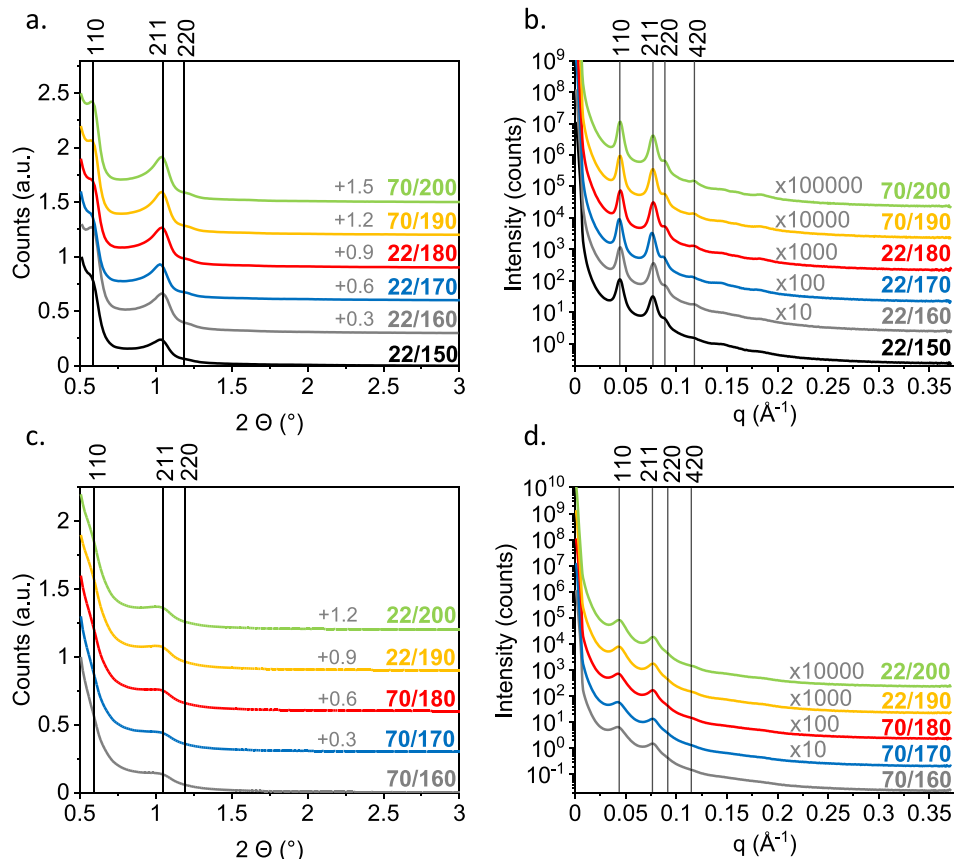


Fig. 1. LA-XRD and SAXS of ordered (a. and b.) and semi-ordered (c. and d.) MFNCO materials.

70/180, 22/190, 22/200), based on the drying (T_d) and calcination (T_c) temperatures (T_d/T_c).

The diffraction patterns obtained by wide angle powder X-ray diffraction (WA-PXRD) depict pure spinel structure for all samples without any additional reflections, even at low calcination temperature of 150 °C (Fig. S3). This suggests a complete conversion of nitrates and the absence of other phases. Crystallite size domains, determined using the Scherrer equation, ranged from 10.3 to 12.7 nm and increased with higher calcination temperatures, which is consistent with prior research (Tab. S5). [42–44] The crystallite sizes calculated from diffraction peak line broadening appear to somewhat ‘outgrow’ the KIT-6 template pore size. However, anisotropic crystal growth is a common feature of nanocast materials. The 3D gyroid KIT-6 structure leads to the formation of a network of slightly curved crystalline rods instead of perfectly spherical crystallites, which explains the observed differences. The HR-TEM images (Fig. 2b, e) display the pore size and wall thickness of the nanocasts and the non-spherical shape of the crystallites and further prove the inverse replication of the KIT-6 pore structure.

HR-EDX elemental mapping was conducted on samples 22/150 and 70/200, representing the lowest and highest synthesis temperatures, respectively. The mapping results confirmed uniform elemental distribution in these samples and indicated that the other samples will likely exhibit uniform elemental distributions as well (Fig. S4–5).

While the replication of the KIT-6 framework was successful in all cases and the 3-D gyroid-like replica structure became visible in the HR-SEM, a clear change in catalyst particle size and shape is evident, when comparing the ordered materials with the semi-ordered materials (as judged from LA-PXRD and SAXS). HR-SEM images of ordered materials (Fig. 3) show that large domains of the KIT-6 pore network were replicated and that the resulting particles inherited a mostly spherical shape and a size of roughly 300 – 500 nm. Dynamic light scattering (DLS) (shown in Fig. S6–8; Tab. S6) was used to measure the hydrodynamic diameters (Z-average) of the ordered MFNCO materials, which were found to be in the range of 308–564 nm. HR-SEM revealed that in semi-ordered materials (Fig. S9), comparably small KIT-6 domains were successfully replicated, resulting in smaller particles which were

unevenly shaped and ranged from 50 to 100 nm in size. DLS results confirmed these findings, showing a narrow hydrodynamic diameter range (136 – 162 nm) for the semi-ordered materials, except for the 70/160 sample, which had a diameter of 266 nm. We used high resolution transmission electron microscopy (HR-TEM) to examine the 22/150 and 70/200 samples in more detail, and confirmed that the mesopores were highly ordered, with pore diameters of approximately 6.5 nm and a gyroid pore structure (Fig. 2). The particles of the 22/150 sample ranged from approximately 300 – 500 nm, while those of the 70/200 sample were in a broader range of 150 – 600 nm. Furthermore, the crystal plane spacings highlighted in Fig. 2b and e, matched very well with the spinel oxide lattice planes determined by PXRD and the crystalline domain sizes are comparable to the calculated values obtained using the Scherrer equation (Tab. S5).

3.3. Porosity

The nitrogen adsorption–desorption isotherms measured at –196 °C show type IV isotherms with two distinct H2b hysteresis loops, resulting in a well-defined bimodal NLDFT pore size distribution for the ordered MFNCO materials (Fig. 4a, b). The formation of the secondary pore size can be corroborated with the previously mentioned 110 reflections observed in SAXS and LA-XRD measurements (Fig. 1). We tentatively assign this feature mainly to the replication of only one of the two KIT-6 subframeworks in some domains of the nanocasts (i.e., *heterogeneous filling*), leading to the formation of such large secondary mesopores. Additionally, the formation of large mesopores in the metal oxides due to a shift/displacement of the gyroid (non-intersecting) sublattices is also possible. [39] In contrast, the semi-ordered samples exhibit a N₂ physisorption isotherm with a broad hysteresis loop at high relative pressures, indicating a relatively non-uniform, broad pore size distribution with a shift towards bigger pores (Fig. 4c, d). As DLS measurements revealed, the particle size of the semi-ordered samples was distinctively smaller, and we conclude that this led to the increased total pore volume due to a higher interparticle gas condensation contribution. Nevertheless, the SSA resides in a narrow range of 121 – 153 m² g⁻¹ for

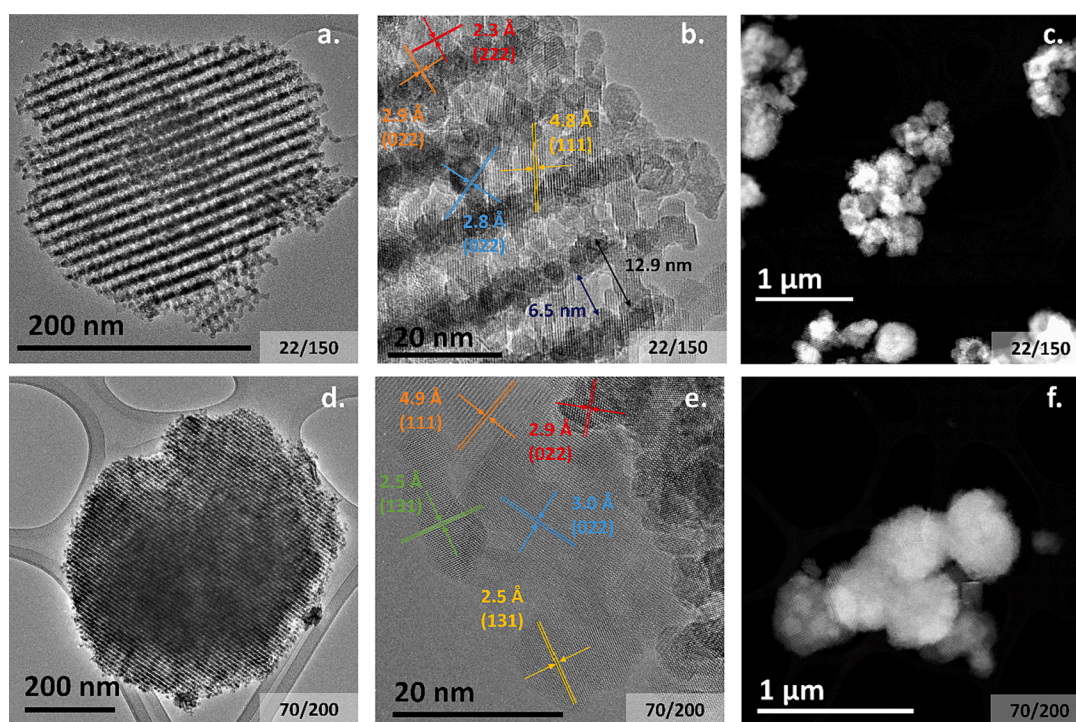


Fig. 2. HR-Transmission electron microscopy (HR-TEM) images of 22/150 (a and b) and 70/200 (d and e) depicting the characteristic spinel crystal planes, and scanning TEM (STEM) images (c and f).

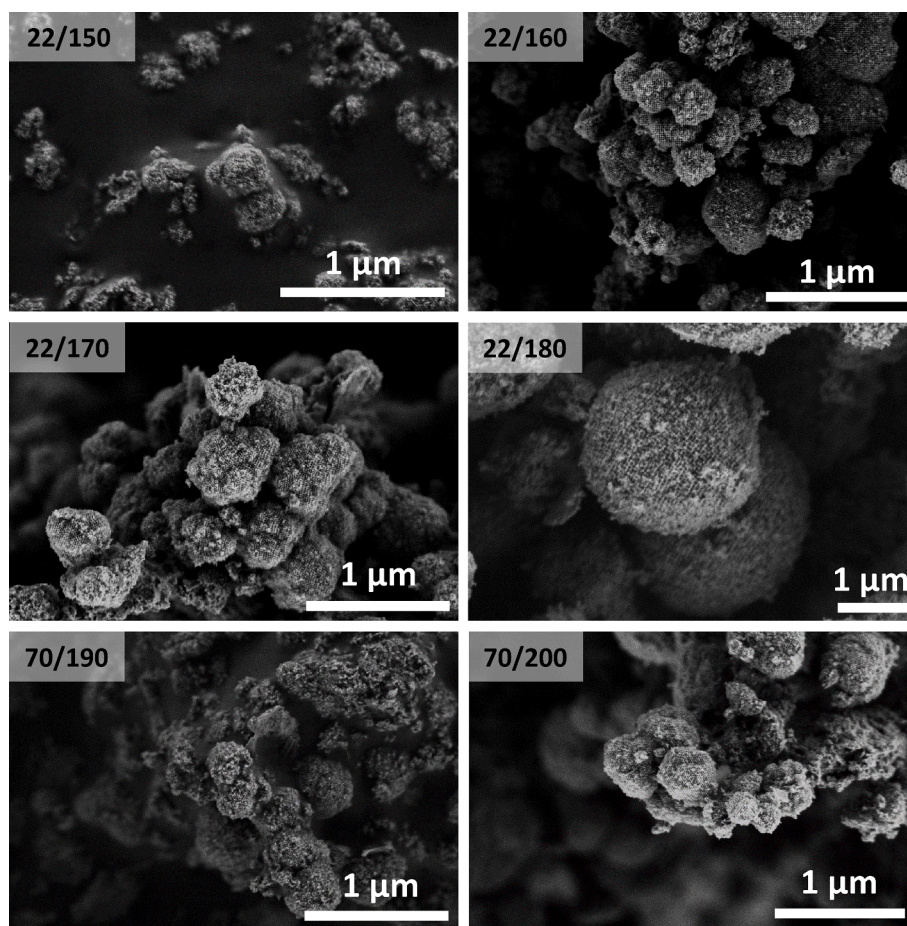


Fig. 3. HR-SEM images of ordered MFNCO catalysts.

all samples, only slightly increasing with decreasing calcination temperature (Tab. S1).

For the sake of comparison and as a potentially cheaper alternative, commercially available silica gel was also utilized as a hard template for the one-step impregnation nanocasting synthesis of MFNCO. Even though lacking the 3D-ordered mesopore geometry and the narrow pore size distribution offered by KIT-6, the plain silica gel yielded a comparable porosity (BET SSA of $493 \text{ m}^2 \text{ g}^{-1}$, NLDFT pore size of 7.0 nm, and total pore volume of $0.80 \text{ cm}^3 \text{ g}^{-1}$, (Fig. S1; Tab. S1). Here, pre-drying at 22 and 70°C was followed by calcination at 170 and 200°C , respectively (22/170 SG and 70/200 SG). Nitrogen physisorption isotherms and the corresponding NLDFT pore size distributions of the silica gel-templated MFNCO samples reveal similar porosity for both samples. They exhibit a dominant pore size centered at 5.7 nm, but the pore size distribution is rather broad, which was likely inherited from the disordered silica gel template but could also be caused by additional interparticle gas condensation. (Fig. S10a, b). For both samples, the SSA was in the same range as that of the nanocasts obtained from KIT-6 templating and the materials also exhibited similar pore volumes as the ordered MFNCO materials (Tab. S1). As expected, LA-PXRD and SAXS confirmed the absence of mesopore ordering, whilst the HR-SEM micrograph of 70/200 SG depicts agglomerated, highly porous particles exhibiting irregular shapes and sizes (Fig. S10c, d; Fig. 5). DLS measurements of the non-ordered, silica gel-templated MFNCO samples yielded an average hydrodynamic diameter of 130 nm for both samples (Fig. S6; S8; Tab. S6).

Overall, pre-drying and calcination temperatures in the nanocasting synthesis seem to determine the morphology of the replicas. Depending on these conditions, either spherical particles with roughly 200 – 600 nm in diameter, highly ordered mesopores, and bimodal pore size distribution or rather small (roughly 50 – 100 nm), irregularly shaped,

catalysts with semi-ordered mesopores can be obtained. Furthermore, using a mesoporous silica gel as a hard template resulted in non-ordered, small particles of around 130 nm in hydrodynamic diameter with SSAs, pore sizes, and pore volumes comparable to KIT-6 templated nanocasts. Based on the results from TEM, HR-SEM, N_2 physisorption, LA-PXRD, and SAXS, the following sample classification is possible: the ordered (22/150, 22/160, 22/170, 22/180, 70/190, and 70/200), semi-ordered (70/160, 70/170, 70/180, 22/190, and 22/200), and non-ordered (22/170 SG, 70/200 SG) MFNCO materials.

These findings highlight the drastic influence of the pre-drying/calcination temperature couple on the replication process. We expect that the energetically favored decrease in surface free energy caused by the accumulation in large spherical domains within the KIT-6 pore network, rather than filling small nanodomains, is the reason why the slight variations in the synthesis had such an apparent effect on the textural properties of the materials as observed in the case of the ordered vs. semi-ordered MFNCO samples. Stucky *et al.* reported that the calcination in the semi-sealed crucibles leads to a humid and highly corrosive (NO_x) atmosphere, allowing melting and rearrangement of precursors and reaction intermediates. This might result in a temporary semi-equilibrium of deposition, dissolution, rearrangement, and redeposition until the volatile gasses eventually escape from the semi-sealed containers and the metal oxide is formed. [29] In our case, the differences between the ordered and semi-ordered materials might be linked to whether or not the suitable conditions for the formation of such a temporal equilibrium are met. It was shown by De Jongh *et al.* for LiBH_4 , that an appropriate stabilizing environment can enable the infiltration of SBA-15 silica mesopores and lead to long range ordered materials. [45] This ‘stabilization’ could be transposed to the corrosive environment inside our calcination crucibles which kept reactants in a liquid

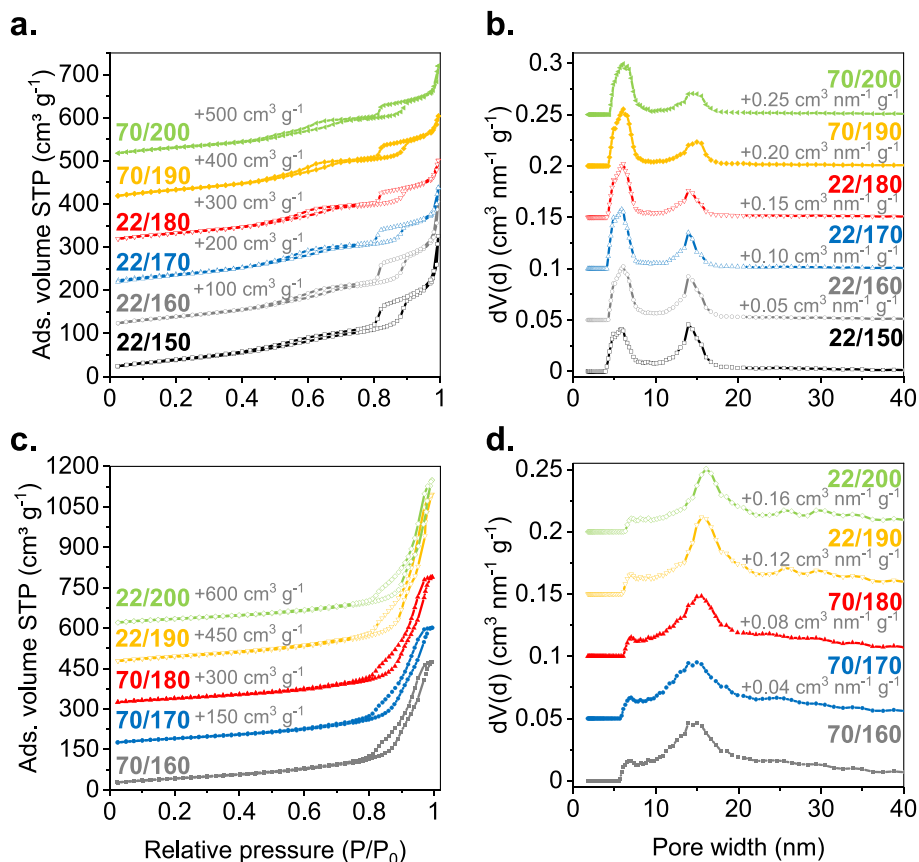


Fig. 4. Nitrogen physisorption isotherms recorded at $-196\text{ }^{\circ}\text{C}$ of ordered (a) and semi-ordered (c) MFNCO materials and respective NLDFT pore size distributions (b and d). Symbols (empty / filled) represent the pre-drying temperature ($22\text{ }^{\circ}\text{C}$ / $70\text{ }^{\circ}\text{C}$).

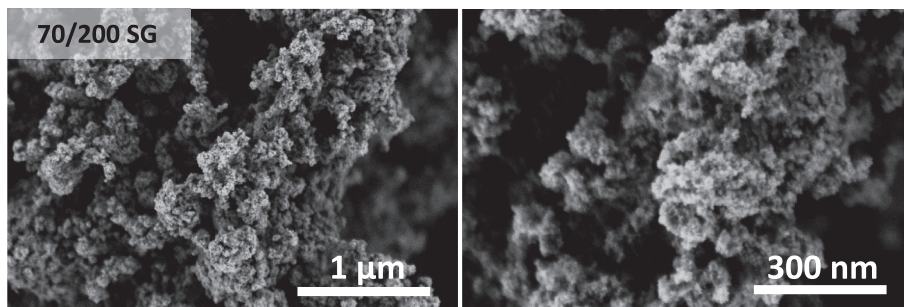


Fig. 5. HR-SEM image of silica gel templated MFNCO (70/200 SG).

state for an extended time and decelerated solidification. The H_2O and NO_x nitrate salt decomposition products were attributed to lead to the agglomeration of supported Ni and Co_3O_4 catalyst particles. [46,47] As we elaborated in the previous sections, we observed that the pre-drying, which affects the crystal water content in the nitrate salt precursors, had a significant effect on the texture of the final materials. Hence, we assume that during the calcination, the additional crystal water retention for the samples dried at room temperature results in high humidity inside the semi-sealed calcination crucible, essentially extending the timeframe where the MFNCO precursors exist in a liquid state. The importance of humidity was studied by De Jong *et al.* who investigated the melt infiltration of $\text{Co}(\text{NO}_3)_2 \cdot 6\text{H}_2\text{O}$ into SBA-15 mesoporous silica in open and closed Teflon containers, and pointed out, that dehydration of the transition metal salt inhibits homogeneous pore-filling. [48] Based on our findings from the TGA measurements we presume that the samples calcined in mild conditions between 150 and $180\text{ }^{\circ}\text{C}$, and hence

in a temperature range of slow nitrate salt decomposition kinetics, additionally maintained a semi-equilibrium of precipitation and redissolution for a longer time. As a consequence, the facilitated mobility of precursors and intermediates and the extended duration of the semi-equilibrium eventually led to the energetically favored rearrangement and merging of filled nanodomains into larger spherical domains. This might explain the formation of comparably large and spherical mixed metal oxide particles with highly-ordered mesopores when performing the pre-drying at room temperature and the calcination in a range between 150 and $180\text{ }^{\circ}\text{C}$ (samples 22/150 – 22/180). We suspect that the higher calcination temperatures (22/190 – 22/200 $^{\circ}\text{C}$), as demonstrated with the TGA experiments, result in increased nitrate salt dehydration and decomposition rates. This induces a fast rise of water and NO_x vapor pressure inside the semi-sealed container which leads to a faster release of water and NO_x gasses out of the semi-sealed container. Compared to the lower temperatures, the semi-equilibrium time window might be

significantly shorter at the higher temperatures (190 and 200 °C) and again lead to premature solidification of the intermediates. For the materials pre-dried at 70 °C, exhibiting a substantially reduced crystal water content, the slow decomposition at low temperatures (samples 70/160 to 70/180) might lead to almost complete dehydration before the bulk nitrate decomposition sets in and hence limits the rearrangement inside the KIT-6 pores due to the slow but steady escape rate of the remaining water out of the semi-sealed container. Higher calcination temperatures, as shown for samples 70/190 and 70/200, accelerate the nitrate salt decomposition, which in the presence of humidity, can facilitate the rearrangement due to the temporal deposition-dissolution equilibrium. Retention of humidity up to the decomposition temperature of nitrate salts was also attributed to facilitating the hydrolysis reaction of metal nitrate salts as shown in the simplified and generalized Equation (1).



It was reported, that humidity causes increased decomposition kinetics, improved crystallinity, as well as a smoother and less defective surface for the final oxides.[49–52] At some point of the reaction, the formation of a water-HNO₃ azeotrope (32:68 %) with a boiling temperature of 120 °C is likely. This would facilitate the nitrate removal to further shift the hydrolysis reaction to the product side. With the decreasing humidity level inside the semi-sealed calcination crucible, the equilibrium of the subsequent condensation reaction, as indicated in Equation (2), would then continuously shift towards the metal oxide product side. In reality, those conversions were demonstrated to consist of complex multi-step reactions including several hydroxy- and oxynitrate intermediates for single metal systems.[52,53] A further discussion of the formation mechanism for the present nanocast multi-metal system is, however, beyond the scope of this work.

3.4. Spectroscopic characterization of the materials and surfaces

The five characteristic Raman-active vibrational modes as shown by the Raman spectra recorded for all ordered MFNCO materials (Fig. S11; Tab. S7) are characteristic for Co₃O₄ based materials.[15,54–57] For the 70/200 sample, the three F_{2g} modes are located at around 185, 507, and 604 cm⁻¹, and the peaks centered at roughly 464 and 657 cm⁻¹ were identified as E_g and A_{1g} vibrational modes. There are peak shifts between the samples, but no linear temperature-induced trend could be observed. According to literature, crystal defects, -size, and -strain, which can be introduced by element doping or calcination temperature, are amongst the parameters which can influence the vibrational behavior of the metal oxide lattice and often shows in a shift in the A_{1g} band position.[15,54–57] The complex metal matrix, with hardly assignable oxidation states (see XPS section), makes it impossible to clarify the occupation of octahedral or tetrahedral sites within the spinel unit cell with the employed set of materials characterization techniques. This uncertainty, and the inhomogeneous crystallite size make it difficult to draw conclusions on the meaning of the observed peak shifts.[15,18,58]

X-ray photoelectron spectroscopy (XPS) spectra were recorded for the ordered materials (150 – 200 °C) and 22/170 SG. The XPS spectra are displayed in Figures S12 and S13, and the results obtained from quantitative XPS analysis and the evaluation of Co²⁺/Co³⁺ and oxide/hydroxide ratios are summarized in Table S8-10 and discussed in detail in the Supplementary Material. In short, the high-resolution XPS profiles are in good agreement with literature describing XPS spectra of transition metal doped Co₃O₄. They further indicate only minor effects of calcination temperature upon the surface chemistry of the samples. This aligns with our previous study where no major differences were observed between MFNCO prepared at 300 °C with open container and 200 °C with semi-sealed container.[23]

In XPS, X-rays probe the outer few nanometers of a material and only an averaged elemental composition is obtained, while for low energy ion scattering (LEIS) the chemical surface composition of the outmost atomic layer of a material can be determined. In LEIS scattered noble gas ions generate the measured signal. As those detected, scattered Ne⁺ ions effectively show no penetration into the measured substrate, the obtained information concerns only the outmost material surface. LEIS offers valuable and more accurate information on the surface chemistry interacting with the electrolyte in heterogeneous electrocatalytic reactions.[59] The determined chemical surface composition for the materials is given in Fig. 6b and Table S11. Generally, the materials exhibited a higher Fe and Ni surface coverage than expected from nominal composition (83.3 % Co, 10 % Ni, 3.3 % Fe and Mn, respectively) and XRF-quantification (Tab. S4), while Mn levels were comparable to the bulk composition. This might be caused by the SiO₂ template removal procedure with NaOH, which commonly contains contaminants of Fe and Ni that could, to some extent, be deposited on the surface of the catalysts. However, due to the usage of highly pure NaOH we expect this contribution to be small. The low calcination temperature samples 22/150 and 22/160 exhibit a drastically reduced amount of surface Co, whilst Ni and Fe surface coverages were enhanced more than two and fourfold, respectively. For these samples, the high concentrations of Ni and Fe can be explained by residues of nanosized or amorphous oxides and an incomplete formation of the spinel structure. Due to the excellent surface sensitivity of LEIS, they can be detected, even though they do not make up a substantial share of the whole material. Fig. 6a displays that the single peaks for Fe, Ni, Mn, and Co are lying close to each other and are overlapping. To quantify each element reliably, single metal (Fe, Ni, Mn, and Co) oxide standards were measured. To attribute for the special mesoporous surface morphology of the MFNCO samples, the single metal oxide samples were prepared by the same nanocasting process and therefore exhibited a comparable surface morphology. These standards were then used to determine the precise position of each elemental peak, so the contribution of each element could be fitted in the overlapped spectra of the MFNCO samples (fits can be found in Fig. S14). At temperatures above 160 °C, as shown for the 22/170 sample, the surface composition is richer in Co, and closer to the nominal composition, meaning that the spinel formation is completed, and no residual oxide species are left. An alternative explanation would be that the low-temperature samples have a different elemental distribution in the spinel structure. As was shown previously, the surface sensitivity of LEIS allows the determination of the surface termination layer of spinels, which were shown to be terminated by the octahedral site ions for spinel ferrites or ZnCr₂O₄. A certain enrichment of elements in the LEIS spectra could indicate preferential occupation of the octahedral sites.[60,61] Finally, no Si was found by the LEIS measurements, confirming the high efficiency of the Si leaching step, although Na could be detected, remaining from the NaOH leaching agent (Fig. 6a).

3.5. Electrocatalytic OER performance

The alkaline OER performance of the MFNCO catalysts was benchmarked in 1 M KOH following previously published measurement protocols.[23,36,62] Fig. 7 depicts the linear sweep voltammetry (LSV) results of the ordered, semi-ordered, and non-ordered MFNCO materials. Generally, all samples exhibit good OER performance, most of them outperforming the mesoporous Co₃O₄ reference material, which was synthesized under regular nanocasting conditions (KIT-6–40 template, 70 °C pre-drying and 500 °C calcination for 5 h). In the context of our study, mesoporous Co₃O₄ may be considered as viable reference material, which was benchmarked against the state-of-the-art IrO₂ electrocatalyst before.[12,63] In detail, although there are no major differences in the LSV curves due to the chemical similarity of the samples, activity trends induced by calcination temperature, particle size, porosity, crystallite size and/or mesopore ordering, could be observed as summarized in Table S12. The ordered MFNCO materials generally

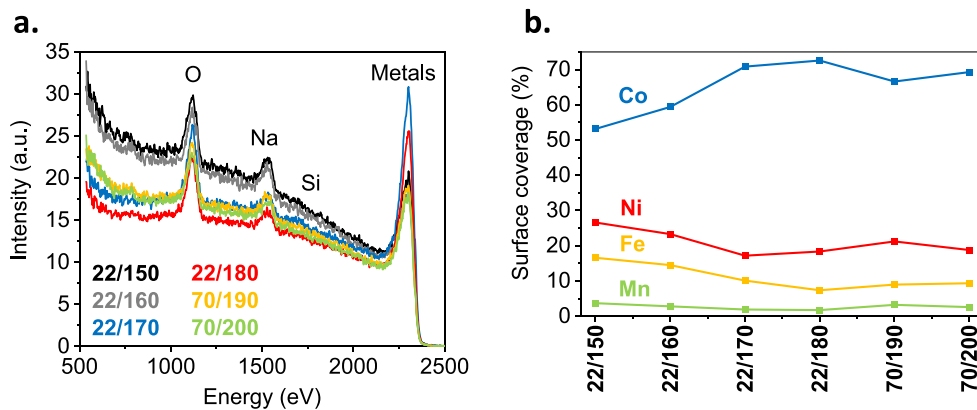


Fig. 6. Low energy ion scattering (LEIS) analysis of ordered MFNCO samples depicting the LEIS survey spectra (a) and metal oxide surface coverage evaluation (b).

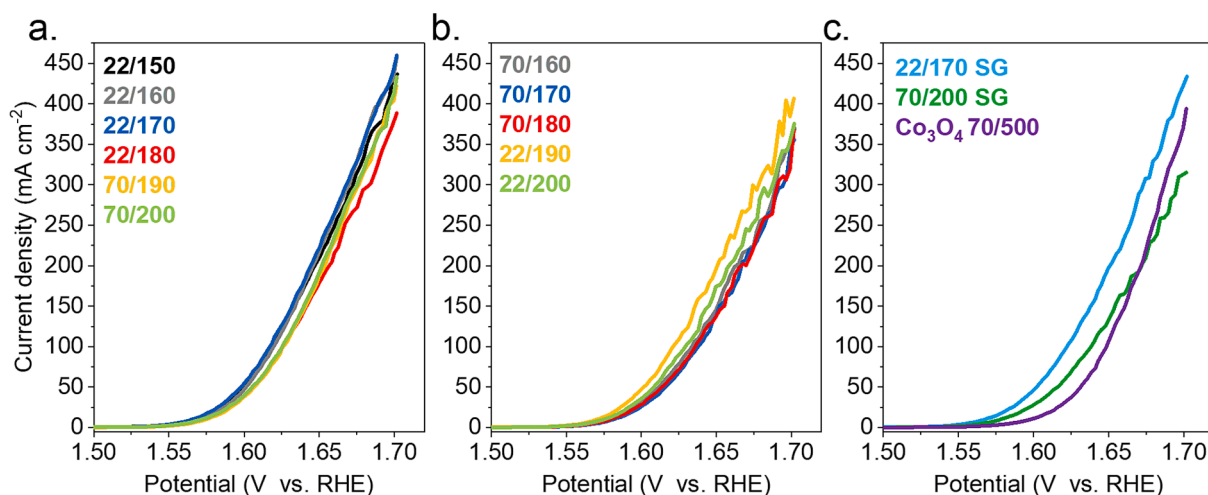


Fig. 7. The current–voltage diagrams obtained from linear sweep voltammetry (LSV) normalized to the geometric electrode area for (a) ordered, (b) semi-ordered, and (c) non-ordered MFNCO materials and Co_3O_4 (70/500) reference.

demonstrated a slightly higher activity towards the OER than the semi-ordered analogs, which was manifested in lower overpotentials and higher current densities at 1.7 V. The catalysts 22/150 and 22/170 exhibited the lowest OER overpotentials (336 and 335 mV, respectively), whilst the ordered catalysts made at 180–200 °C (22/180, 70/190, 70/200) exhibited slightly higher values, with 345 mV being the highest (70/190 sample). At a potential of 1.7 V vs. RHE, the low-temperature calcination samples, but most prominently 22/170, exhibited the highest current densities of 433 (± 10) mA cm^{-2} . This trend is supported by Nyquist plots (Fig. S15) obtained from EIS measurements, which indicate decreased charge transfer resistance for the materials calcined at low temperatures. As displayed in the Bode plots in Figure S16, all MFNCO samples exhibit a single capacitance response in the same low-frequency range between 10^0 and 10^2 Hz, hinting at identical reaction mechanisms and active sites. The Z-shaped impedance magnitude plot is typical of a charge-transfer controlled reaction. [64] The OER kinetics, characterized by the Tafel slope depicted in Figure S17 and Table S12, were in a narrow range between 39 and 43 mV dec^{-1} , indicating improved OER kinetics in comparison to the Co_3O_4 reference (47 mV dec^{-1}). Within the semi-ordered materials, the low-temperature calcination seems to have the adversary effect, since the materials exhibited the highest overpotentials, lowest current densities at 1.7 V, and highest charge transfer resistances (70/160, 70/170, 70/180). Compared to the rather smooth LSV curves recorded for the ordered MFNCO materials, the semi-ordered MFNCO materials are becoming unsteady at current densities above 100 mA cm^{-2} (Fig. 7b).

An explanation for that behavior could be that the ordered mesoporous structure of the MFNCO samples facilitate the diffusion of oxygen gas molecules formed during OER through their highly open pore network. Hence, O_2 accumulation and bubble formation inside the pores, which would block the surface for OER, is reduced. In contrast, the irregular and rough structure of the semi-ordered catalysts might hamper the diffusion of the oxygen molecules, effectively causing fluctuations of accessible surface area due to more extensive bubble formation inside the pores, thus leading to unsteady current measurements. Besides displaying comparable physicochemical properties, the non-ordered 22/170 SG material obtained from silica gel templating exhibited very similar activity for OER to the ordered and best performing KIT-6-templated counterpart 22/170 (Fig. 7c, Tab. S12). The 70/200 SG was following the trend of decreased activity for OER and ranked amongst the worst MFNCO catalysts. (Fig. 7c, Tab. S12). The silica gel-made MFNCO samples did therefore not only confirm the electrocatalytic OER activity trend observed for the samples prepared using a KIT-6 hard template, but they also showed that nanocasting is not restricted to the replication of expensive, highly ordered model materials, and could also be applied on cheap commercially available silica gel. Cyclic voltammetry was performed for three cycles and Figures 8 and S18 depict the 1st and 3rd cycle. The anodic and cathodic peaks were assigned to $\text{Co}^{2+}/\text{Co}^{3+}$ (A1/C1), $\text{Co}^{3+}/\text{Co}^{4+}$ (A2/C2), $\text{Ni}^{2+}/\text{Ni}^{3+}$ and Ni^{4+} (A3/C3) redox reactions. [23] In the first CV cycle, the main redox reactions are expected to originate from cobalt due to its prevalence, but contributions from the doping elements Ni, Fe, and Mn are likely. Compared to plain Co_3O_4 , a

clear influence of doping elements on the redox peak positions is obvious, as they shifted them to lower potentials for all MFNCO materials (Fig. 8). Furthermore, the increased peak areas indicate a higher number of electroactive species. Such a significant change in the CV shape suggests strong electronic interactions between the metals within the spinel structure, as this technique is surface sensitive. Within the ordered MFNCO materials (Fig. 8a), a decrease in calcination temperature led to two effects in the A1 and A2/A3 oxidation potentials: (1) the oxidation peaks were shifted to higher potentials and (2) the peak areas were affected. The A1 low-intensity oxidation peak, which can be attributed to the oxidation of Co^{2+} to Co^{3+} , was most pronounced for the 22/180 and 70/190 samples, indicating a higher amount of Co^{2+} sites on the surface of those materials.[55] Contrary to the trend observed by XPS, the CV curves of the 22/150 and 22/170 samples indicate comparably low oxidation of Co^{2+} sites while at the same time also the most pronounced $\text{Co}^{3+}/\text{Co}^{4+}$ oxidation. For many years Co^{4+} was postulated as the main active site in alkaline OER.[55,65,66] However, in recent years, Co^{2+} species were also proposed to act as the active sites for OER, as was the subsequential Co^{2+} oxidation to an intermediate Co^{3+} and finally Co^{4+} . [67,68] Consequently, we can only presume that the superior OER performance and the enhanced abundance of Co^{4+} sites in our MFNCO 22/150 and 22/170 samples are linked. We further observed an anodic shift in the A2/3 oxidation peak potential, which occurred with decreasing calcination temperatures. Such a shift was reported to originate from Fe incorporation (intentional or by contaminations) into Co and Ni oxide-based catalysts previously.[9,24,69,70] Moreover, according to the LEIS results discussed above, the lower calcination temperatures led to an increased amount of manganese, nickel and iron in the catalysts' surface layer. The accumulation of those elements on the surface layer might also increase the number of suitable sites for the Fe adsorption from the electrolyte, which could be another reason the above-mentioned shift. Activation of nickel cobalt oxides by iron substitution or electrolyte impurities was described before, and an increased amount of Ni and Fe species in the surface layer of the samples calcined at lower temperatures could therefore be one of the reasons for their improved activity.[24,71,72] In the third CV cycle (Fig. S18), the anodic and cathodic scans become increasingly similar in between the MFNCO samples. A reversible peak was found at 1.2 V vs RHE, which might be linked to the A1/C1 redox processes. Additionally, the A2/3-C2/3 pair was similar to the one recorded in the first CV cycle. Within the ordered samples (Fig. S18a), the low calcination temperature samples (150 – 180 °C) have a higher current response to the A1/C1 redox-reaction, which could imply that those materials retain more Co^{2+} species than the MFNCO samples calcined at 190 and 200 °C.

The electrochemical active surface area (ECSA) was determined at 1.05 V vs. RHE after cycling at various sweep rates (20 – 180 mV s^{-1}) in the range between 1.0 and 1.1 V (Fig. S19-21, Table S13). In our case, the CV scans exhibit an asymmetric shape which indicates a pseudocapacitor behavior due to the presence of faradaic reactions. As a result, the fit of capacitive current difference vs. applied scan rate shows nonlinearity. The pseudocapacitive behavior for Co_3O_4 , NiCo_2O_4 , and other TMOs has already been reported.[74–76] The linearity of the capacitive current vs. applied scan rate also did not improve when performing the CV measurements in a lower potential range 0.5 – 0.8 V. (Fig. S22). Therefore, we decided to use the allometric fit to compensate for the non-ideality of our system.[73] The double layer capacitance (C_{dl}) and ECSA, which were calculated by applying linear and allometric fits are summarized in Tables S13-14, and displayed in Figures S23-25. Unless stated otherwise, we always refer to the ECSA determined by the allometric fit. The highest ECSA was observed for the 70/200 sample, and despite the uncertainty linked to the pseudocapacitive behavior, the ECSA of the samples is clearly reduced with decreasing calcination temperature. In Figure S26, we graphically correlated the ECSA values, the position of the precatalytic A2/3 oxidation peak, and the OER overpotential for the group of the ordered MFNCO samples. The observed precatalytic anodic A2/3 peak shift is accompanied by a

decrease in charge transfer resistance (Table S12), and thus faster diffusion-controlled redox processes and a lower overpotential, which supports the formation of more active sites when performing the calcination at low temperatures (150 – 170 °C).

As a measure of the intrinsic catalyst activity, we normalized the LSV plots and current densities at 1.7 V to the ECSA (Fig. S27; S28a). Due to their lower ECSA, the intrinsic activities are clearly increased for the low-temperature (150 – 170 °C) calcination samples. We could observe this trend for ordered, semi- and non-ordered MFNCO samples. Interestingly, the normalization to the specific surface area (SSA), attributed the highest activity to the oxides calcined at 190 and 200 °C for the ordered and semi-ordered MFNCO samples (Fig. S29; S28a). As the ECSA and SSA values follow opposite trends, we suggest their ratio as one of the parameters to evaluate the intrinsic activity of the catalysts' surface as depicted in Figure S28b. Even though the samples calcined at lower temperatures have a comparably low amount of accessible active sites per cm^2 of their SSA, the initial activity of these sites is sufficient to reach the highest current densities. On the contrary, Figure S28 displays that, despite the higher ECSA, the activity of the surface sites of the 70/190 and 70/200 samples is much lower. In summary, reducing the calcination temperature to 150 – 170 °C appears to enable the formation of a catalytically more active MFNCO surface. Further work can be directed towards improving the accessibility and increasing the number of these highly active surface sites of the mixed metal oxides.

Chronopotentiometry (CP) (Fig. 9a) performed for MFNCO 22/170 and 70/200 revealed excellent stability of both catalysts and even activity enhancement during the first hours of operation. MFNCO 22/170 proved to be the more active and more stable catalyst, essentially displaying almost no degradation during the 22 h of CP. ICP-MS was used to monitor the metal ion concentration throughout the stability tests (Tab. S2, Fig. 9c and d). We observed similar trends for both samples, but the 22/170 sample exhibited less initial Fe and Mn dissolution than the 70/200 sample. In detail, the first electrolyte sample, taken directly after the start of the CP measurement, displayed an increase in Mn, Fe, Co, and Ni concentration in the electrolyte (with respect to the concentrations present in the native 1 M KOH). This suggests an initial dissolution of the catalyst once in contact with the electrolyte and/or at the beginning of the electrochemical reaction. As the CP experiment progressed, the Mn and Ni concentrations stayed relatively stable throughout the stability tests, whilst Fe and Co concentrations gradually decreased, suggesting a metal (re-)deposition within the system. For Fe, this decrease was particularly pronounced, and we could observe that the Fe level dropped by more than 60 % below the amount of Fe contaminations inside the native 1 M KOH electrolyte. Activation of Ni in nickel cobalt oxides by the presence of trace amounts of Fe in the electrolyte was described before, and corroborates the observed activation of our catalysts which manifests in a decrease of the potential to achieve 10 mA cm^{-2} during the CP stability test.[24,37] XPS and powder XRD measurements were performed before (pre) and after (post) the CP and the similarity of the results in terms of surface and bulk compositions is another indication of the excellent stability of the electrocatalysts (Fig. S30, Table S15, Fig. 9b).

4. Conclusion

In this contribution, we investigated the influence of pre-drying (22 vs. 70 °C) and calcination temperature (150 – 200 °C) on the formation of nanocast $\text{Mn}_{0.1}\text{Fe}_{0.1}\text{Ni}_{0.3}\text{Co}_{2.5}\text{O}_4$ in semi-sealed calcination containers and tested the obtained materials for the alkaline OER. We observed that the employed pre-drying temperature, which is effectively influencing the crystal water content, and the calcination temperature, which affects the decomposition kinetics of the nitrate salts, had significant effects on mesopore ordering, particle size, and shape of the nanocast replicas. Through adjustments of the pre-drying temperature, highly ordered mesoporous, spherical, mixed metal oxide particles ranging between 300 and 500 nm and exhibiting a well-defined bimodal pore size

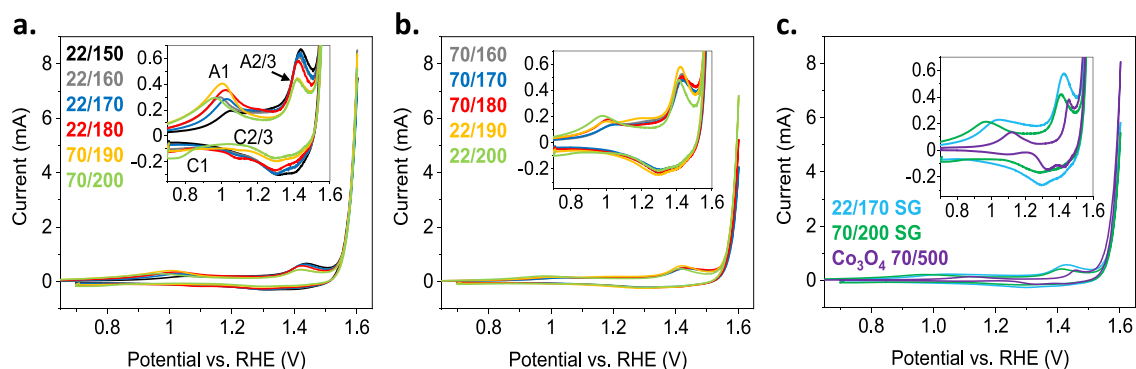


Fig. 8. Cyclic voltammograms (1st cycle) of ordered (a), semi-ordered (b), and non-ordered (c) MFNCO catalysts.

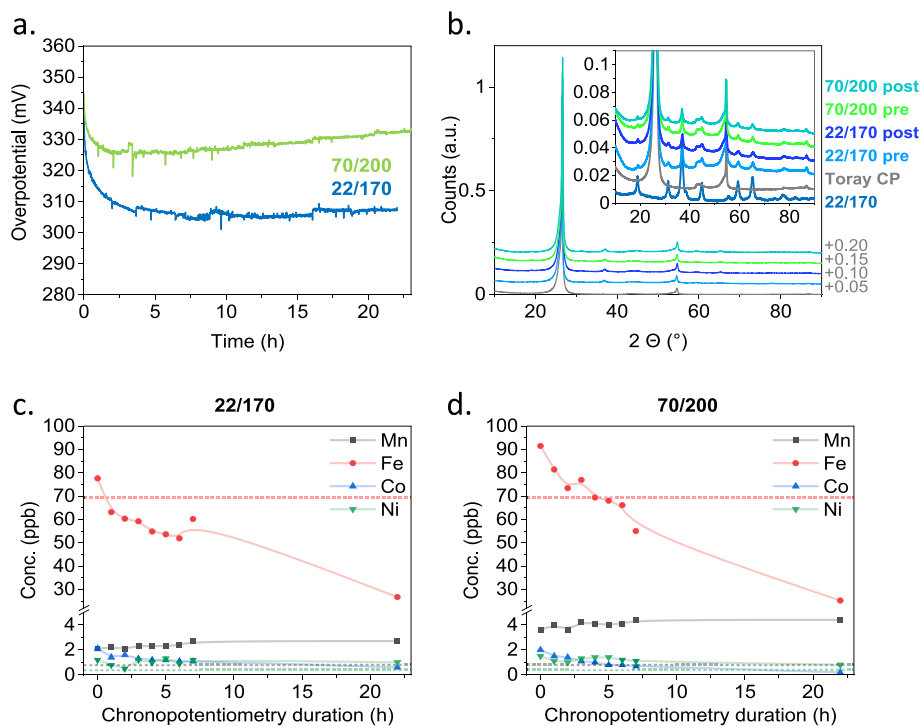


Fig. 9. Chronopotentiometry performed with MFNCO 22/170 and 70/200 catalysts supported on carbon paper at 25 °C employing 10 mA cm⁻² for over 22 h (a), the corresponding XRD patterns before (pre) and after (post) CP (b), and the ICP-MS analysis depicting the Mn, Fe, Ni, and Co concentrations in the 1 M KOH electrolyte throughout the CP duration for MFNCO 22/170 (c) and 70/200 (d). The dotted lines correspond to the metal ion concentrations in plain 1 M KOH.

distribution, and high SSA could be obtained in the full calcination temperature range. Interestingly, a mismatch of pre-drying and calcination temperature led to semi-ordered, small, irregularly shaped particles. We conclude that the rearrangement of molten nitrate salts and intermediates inside the pores of the template into bigger domains was enabled by the interplay of humidity, nitrate salt decomposition kinetics (as determined by the calcination temperature) and gas escape rates (semi-sealed container). Even though we employed calcination temperatures, which are far below the typically used ones for mixed metal oxides, PXRD, Raman spectroscopy, elemental mapping, and XPS indicated phase-pure spinel structure, homogeneous elemental distribution, and comparable surface chemistry for all MFNCO samples. LEIS revealed that calcination temperatures of only 150 – 160 °C led to a significant increase in Fe-, and Ni- doping elements on the outmost surface layer. The MFNCO electrocatalysts exhibited high activity for the alkaline OER and even though chemically very similar, the highly ordered, spherical catalysts outperformed the semi-ordered analogs. The best OER performance and excellent stability over 22 h was achieved by the sample

calcined at 170 °C. Cyclic voltammetry depicted an anodic shift of the A2/3 oxidation peaks with decreasing calcination temperatures. We interpret this trend as an additional indication of the accumulation of Fe, Ni and Mn in the surface layer of the catalyst. Furthermore, the higher intrinsic current densities highlighted the beneficial effects the low temperature calcination had on the activity towards the OER. Additionally, we could demonstrate that a comparably cheap commercial silica gel was well suited as a hard template for the synthesis of nanocast mixed metal oxides and led to highly active electrocatalysts. Hereby we open the possibility for an economic scaling-up of the synthesis of mesoporous mixed metal oxides via low-temperature calcination.

CRediT authorship contribution statement

Patrick Guggenberger: Writing – original draft, Methodology, Investigation, Formal analysis, Data curation, Conceptualization. **Tatiana Priamushko:** Writing – review & editing, Methodology, Investigation, Formal analysis, Conceptualization. **Prathamesh Patil:** Writing

– review & editing, Investigation, Formal analysis, Data curation. **Jus-tyna Florek**: Writing – review & editing, Investigation, Formal analysis, Data curation. **Daniel Garstener**: Writing – review & editing, Investigation, Formal analysis, Data curation. **Andreas Mautner**: Writing – review & editing, Formal analysis. **Jae Won Shin**: Writing – review & editing, Formal analysis. **Ryong Ryoo**: Validation, Resources. **Christian M. Pichler**: Writing – review & editing, Resources, Investigation, Formal analysis. **Freddy Kleitz**: Writing – review & editing, Validation, Supervision, Resources, Project administration, Methodology, Formal analysis, Conceptualization.

Declaration of Competing Interest

The authors declare that they have no known competing financial interests or personal relationships that could have appeared to influence the work reported in this paper.

Data availability

Data will be made available on request.

Acknowledgement

The authors acknowledge the funding support of the University of Vienna (Austria). Financial support from the Gesellschaft für Forschungsförderung Niederösterreich (FTI21-D-002) and the European Regional Development Fund (EFRE REACT, WST3-F-542638/004-2021) are gratefully acknowledged. We thank Dr. Jeong-Chul Kim for helping with the SEM measurements. The authors acknowledge additional support (for TEM and SEM measurements) for this work from the Institute for Basic Science (IBS) under grant number IBS-R004 (Republic of Korea).

Appendix A. Supplementary data

Supplementary data to this article can be found online at <https://doi.org/10.1016/j.jcis.2024.01.056>.

References

- [1] International Energy Agency. *Net Zero by 2050: A Roadmap for the Global Energy Sector*; 2021.
- [2] IRENA. *World Energy Transitions Outlook 2023–1.5°C Pathway - Preview 2023*.
- [3] K. Du, L. Zhang, J. Shan, J. Guo, J. Mao, C.C. Yang, C.H. Wang, Z. Hu, T. Ling, Interface engineering breaks both stability and activity limits of RuO₂ for sustainable water oxidation, *Nat. Commun.* 13 (1) (2022) 1–9, <https://doi.org/10.1038/s41467-022-33150-x>.
- [4] C. Felix, T. Maiyalagan, S. Pasupathi, B. Bladergroen, V. Linkov, Synthesis, characterisation and evaluation of IrO₂ based binary metal oxide electrocatalysts for oxygen evolution reaction, *Int. J. Electrochem. Sci.* 7 (12) (2012) 12064–12077, [https://doi.org/10.1016/s1452-3981\(23\)16526-6](https://doi.org/10.1016/s1452-3981(23)16526-6).
- [5] S. Cherevko, S. Geiger, O. Kasian, A. Mingers, K.J.J. Mayrhofer, Oxygen evolution activity and stability of iridium in acidic media. Part 1. - metallic iridium, *J. Electroanal. Chem.* 773 (2016) 69–78, <https://doi.org/10.1016/j.jelechem.2016.04.033>.
- [6] M. Tariq, Y. Wu, C. Ma, M. Ali, W.Q. Zaman, Z. Abbas, K.S. Ayub, J. Zhou, G. Wang, L. mei Cao, J. Yang, Boosted up stability and activity of oxygen vacancy enriched RuO₂/MoO₃ mixed oxide composite for oxygen evolution reaction, *Int. J. Hydrogen Energy* 45 (35) (2020) 17287–17298, <https://doi.org/10.1016/j.ijhydene.2020.04.101>.
- [7] D. Escalera-López, S. Czioska, J. Geppert, A. Boubnov, P. Röse, E. Saraç, U. Kreuer, J.D. Grunwaldt, S. Cherevko, Phase- and surface composition-dependent electrochemical stability of Ir-Ru nanoparticles during oxygen evolution reaction, *ACS Catal.* 11 (15) (2021) 9300–9316, <https://doi.org/10.1021/acscatal.1c01682>.
- [8] H. Osgood, S.V. Devaguptapu, H. Xu, J. Cho, G. Wu, Transition metal (Fe, Co, Ni, and Mn) oxides for oxygen reduction and evolution bifunctional catalysts in alkaline media, *Nano. Today* 11 (5) (2016) 601–625, <https://doi.org/10.1016/j.nantod.2016.09.001>.
- [9] L. Trotochaud, S.L. Young, J.K. Ranney, S.W. Boettcher, Nickel-Iron oxyhydroxide oxygen-evolution electrocatalysts: the role of intentional and incidental iron incorporation, *J. Am. Chem. Soc.* 136 (18) (2014) 6744–6753, <https://doi.org/10.1021/ja502379c>.
- [10] Q. Zhao, Z. Yan, C. Chen, J. Chen, spinels: controlled preparation, oxygen reduction/evolution reaction application, and beyond, *Chem. Rev.* 117 (15) (2017) 10121–10211, <https://doi.org/10.1021/acs.chemrev.7b00051>.
- [11] H. Tüysüz, Y.J. Hwang, S.B. Khan, A.M. Asiri, P. Yang, Mesoporous Co₃O₄ as an electrocatalyst for water oxidation, *Nano Res.* 6 (1) (2013) 47–54, <https://doi.org/10.1007/s12274-012-0280-8>.
- [12] Y.J. Sa, K. Kwon, J.Y. Cheon, F. Kleitz, S.H. Joo, Ordered mesoporous Co₃O₄ spinels as stable, bifunctional, noble metal-free oxygen electrocatalysts, *J. Mater. Chem. A* 1 (34) (2013) 9992–10001, <https://doi.org/10.1039/c3ta11917c>.
- [13] L. Fang, Z. Jiang, H. Xu, L. Liu, Y. guan, X. Gu, Y. Wang, Crystal-Plane engineering of NiCo₂O₄ electrocatalysts towards efficient overall water splitting, *J. Catal.* 357 (2018) 238–246, <https://doi.org/10.1016/j.jcat.2017.11.017>.
- [14] Y. Li, P. Hasin, Y. Wu, Ni_xCo_{3-x}O₄ nanowire arrays for electrocatalytic oxygen evolution, *Adv. Mater.* 22 (17) (2010) 1926–1929, <https://doi.org/10.1002/adma.200903896>.
- [15] H. Du, W. Pu, C. Yang, Morphology control of Co₃O₄ with nickel incorporation for highly efficient oxygen evolution reaction, *Appl. Surf. Sci.* 2021 (541) (2020) 148221, <https://doi.org/10.1016/j.apsusc.2020.148221>.
- [16] T. Grewe, X. Deng, H. Tüysüz, Influence of Fe doping on structure and water oxidation activity of nanocast Co₃O₄, *Chem. Mater.* 26 (10) (2014) 3162–3168, <https://doi.org/10.1021/cm5005888>.
- [17] A. Amirzhanova, N. Akmanşen, I. Karakaya, Ö. Dag, Mesoporous MnCo₂O₄, NiCo₂O₄, and ZnCo₂O₄ thin-film electrodes as electrocatalysts for the oxygen evolution reaction in alkaline solutions, *ACS Appl. Energy Mater.* 4 (3) (2021) 2769–2785, <https://doi.org/10.1021/acsaem.1c00064>.
- [18] C. He, X. Han, X. Kong, M. Jiang, D. Lei, X. Lei, Fe-Doped Co₃O₄@C nanoparticles derived from layered double hydroxide used as efficient electrocatalyst for oxygen evolution reaction, *J. Energy Chem.* 32 (2019) 63–70, <https://doi.org/10.1016/j.jechem.2018.06.014>.
- [19] D. Wang, Z. Liu, S. Du, Y. Zhang, H. Li, Z. Xiao, W. Chen, R. Chen, Y. Wang, Y. Zou, S. Wang, Low-Temperature synthesis of small-sized high-entropy oxides for water oxidation, *J. Mater. Chem. A* 7 (42) (2019) 24211–24216, <https://doi.org/10.1039/c9ta08740k>.
- [20] T. Priamushko, R. Guillet-Nicolas, M. Yu, M. Doyle, C. Weidenthaler, H. Tüysüz, F. Kleitz, Nanocast mixed Ni-Co-Mn oxides with controlled surface and pore structure for electrochemical oxygen evolution reaction, *ACS Appl. Energy Mater.* 3 (6) (2020) 5597–5609, <https://doi.org/10.1021/acsaem.0c00544>.
- [21] J. Sun, H. Li, Y. Huang, Z. Zhuang, CoFeW ternary oxides nanoparticles for oxygen evolution reaction, *Mater. Lett.* 223 (2018) 246–249, <https://doi.org/10.1016/j.matlet.2018.04.018>.
- [22] J. Chen, H. Li, Z. Pei, Q. Huang, Z. Yuan, C. Wang, X. Liao, G. Henkelman, Y. Chen, L. Wei, Catalytic activity atlas of ternary Co-Fe-V metal oxides for the oxygen evolution reaction, *J. Mater. Chem. A* 8 (31) (2020) 15951–15961, <https://doi.org/10.1039/d0ta04088f>.
- [23] T. Priamushko, P. Guggenberger, A. Mautner, J. Lee, R. Ryoo, F. Kleitz, Enhancing OER Activity of Ni/Co Oxides via Fe/Mn substitution within tailored mesoporous frameworks, *ACS Appl. Energy Mater.* 5 (11) (2022) 13385–13397, <https://doi.org/10.1021/acsaem.2c02055>.
- [24] X. Deng, S. Öztürk, C. Weidenthaler, H. Tüysüz, Iron-Induced activation of ordered mesoporous nickel cobalt oxide electrocatalyst for the oxygen evolution reaction, *ACS Appl. Mater. Interfaces.* 9 (25) (2017) 21225–21233, <https://doi.org/10.1021/acami.7b02571>.
- [25] A.J. Esswein, M.J. McMurdo, P.N. Ross, A.T. Bell, T.D. Tilley, Size-dependent activity of Co₃O₄ nanoparticle anodes for alkaline water electrolysis, *J. Phys. Chem. C* 113 (33) (2009) 15068–15072, <https://doi.org/10.1021/jp904022e>.
- [26] F. Yang, D. Deng, X. Pan, Q. Fu, X. Bao, Understanding nano effects in catalysis, *Natl. Sci. Rev.* 2 (2) (2015) 183–201, <https://doi.org/10.1093/nsr/nw024>.
- [27] H. Yen, Y. Seo, R. Guillet-Nicolas, S. Kaliaguine, F. Kleitz, One-Step-impregnation hard templating synthesis of high-surface-area nanostructured mixed metal oxides (NiFe₂O₄, CuFe₂O₄ and Cu/CeO₂), *Chem. Commun.* 47 (37) (2011) 10473–10475, <https://doi.org/10.1039/c1cc13867g>.
- [28] Y. Ren, Z. Ma, P.G. Bruce, Ordered mesoporous NiCoMnO₄: synthesis and application in energy storage and catalytic decomposition of N₂O, *J. Mater. Chem.* 22 (30) (2012) 15121–15127, <https://doi.org/10.1039/c2jm31644g>.
- [29] X. Sun, Y. Shi, P. Zhang, C. Zheng, X. Zheng, F. Zhang, Y. Zhang, N. Guan, D. Zhao, G.D. Stucky, Container effect in nanocasting synthesis of mesoporous metal oxides, *J. Am. Chem. Soc.* 133 (37) (2011) 14542–14545, <https://doi.org/10.1021/ja2060512>.
- [30] J. Haetge, C. Suchomski, T. Brezesinski, Ordered mesoporous MFe₂O₄ (M = Co, Cu, Mg, Ni, Zn) thin films with nanocrystalline walls, uniform 16 nm diameter pores and high thermal stability: template-directed synthesis and characterization of redox active Trevorite, *Inorg. Chem.* 49 (24) (2010) 11619–11626, <https://doi.org/10.1021/ic102052r>.
- [31] C. Simon, J. Timm, D. Tetzlaff, J. Jungmann, U.P. Apfel, R. Marschall, Mesoporous NiFe₂O₄ with tunable pore morphology for electrocatalytic water oxidation, *ChemElectroChem.* 8 (1) (2021) 227–239, <https://doi.org/10.1002/celec.202001280>.
- [32] Y. Xu, J. Jian, F. Li, W. Liu, L. Jia, H. Wang, Porous CuBi₂O₄ photocathodes with rationally engineered morphology and composition towards high-efficiency photoelectrochemical performance, *J. Mater. Chem. A* 7 (38) (2019) 21997–22004, <https://doi.org/10.1039/c9ta07892d>.
- [33] D. Feng, T.N. Gao, M. Fan, A. Li, K. Li, T. Wang, Q. Huo, Z.A. Qiao, A General ligand-assisted self-assembly approach to crystalline mesoporous metal oxides, *NPG Asia Mater.* 10 (8) (2018) 800–809, <https://doi.org/10.1038/s41427-018-0072-z>.

- [34] F. Kleitz, S.H. Choi, R. Ryoo, Cubic *Ia3d* Large mesoporous silica: synthesis and replication to platinum nanowires, carbon nanorods and carbon nanotubes, *Chem. Commun.* 3 (17) (2003) 2136–2137, <https://doi.org/10.1039/b306504a>.
- [35] M. Thommes, K. Kaneko, A.V. Neimark, J.P. Olivier, F. Rodriguez-Reinoso, J. Rouquerol, K.S.W. Sing, Physisorption of gases, with special reference to the evaluation of surface area and pore size distribution (IUPAC Technical Report), *Pure Appl. Chem.* 87 (9–10) (2015) 1051–1069, <https://doi.org/10.1515/pac-2014-1117>.
- [36] C.C.L. McCrory, S. Jung, J.C. Peters, T.F. Jaramillo, Benchmarking heterogeneous electrocatalysts for the oxygen evolution reaction, *J. Am. Chem. Soc.* 135 (45) (2013) 16977–16987, <https://doi.org/10.1021/ja407115p>.
- [37] M. Yu, G. Moon, E. Bill, H. Tüysüz, Optimizing Ni-Fe oxide electrocatalysts for oxygen evolution reaction by using hard templating as a toolbox, *ACS Appl. Energy Mater.* 2 (2) (2019) 1199–1209, <https://doi.org/10.1021/acsaem.8b01769>.
- [38] E. Budiyo, M. Yu, M. Chen, S. Debeor, O. Rüdiger, H. Tüysüz, Tailoring morphology and electronic structure of cobalt iron oxide nanowires for electrochemical oxygen evolution reaction, *ACS Appl. Energy Mater.* 3 (9) (2020) 8583–8594, <https://doi.org/10.1021/acsaem.0c01201>.
- [39] T.W. Kim, F. Kleitz, B. Paul, R. Ryoo, MCM-48-like large mesoporous silicas with tailored pore structure: facile synthesis domain in a ternary triblock copolymer-butanol-water system, *J. Am. Chem. Soc.* 127 (20) (2005) 7601–7610, <https://doi.org/10.1021/ja042601m>.
- [40] T.W. Kim, L.A. Solovyov, Synthesis and characterization of large-pore ordered mesoporous carbons using gyroidal silica template, *J. Mater. Chem.* 16 (15) (2006) 1445–1455, <https://doi.org/10.1039/b516945c>.
- [41] F. Jiao, A.H. Hill, A. Harrison, A. Berko, A.V. Chadwick, P.G. Bruce, Synthesis of ordered mesoporous NiO with crystalline walls and a bimodal pore size distribution, *J. Am. Chem. Soc.* 130 (15) (2008) 5262–5266, <https://doi.org/10.1021/ja710849r>.
- [42] E.O. Nwannebu, N. Abou Harb, R. Gharbi, S. Omanovic, The Effect of calcination temperature on the electrocatalytic activity of Ni–Co–Ir-oxide and Ni–Co–Ru-oxide anodes in the oxygen evolution reaction in alkaline medium, *Solid State Sci.* 119 (April) (2021) 106703, <https://doi.org/10.1016/j.solidstatesciences.2021.106703>.
- [43] R. Itteboina, T.K. Sau, Sol-Gel synthesis and characterizations of morphology-controlled Co₃O₄ particles, *Mater. Today Proc.* 9 (2019) 458–467, <https://doi.org/10.1016/j.matpr.2019.02.176>.
- [44] S.W. Oh, H.J. Bang, Y.C. Bae, Y.K. Sun, Effect of calcination temperature on morphology, crystallinity and electrochemical properties of nano-crystalline metal oxides (Co₃O₄, CuO, and NiO) prepared via ultrasonic spray pyrolysis, *J. Power Sources* 173 (1) (2007) 502–509, <https://doi.org/10.1016/j.jpowsour.2007.04.087>.
- [45] P. Ngene, P. Adelmhelm, A.M. Beale, K.P. De Jong, P.E. De Jongh, LiBH₄/SBA-15 nanocomposites prepared by melt infiltration under hydrogen pressure: synthesis and hydrogen sorption properties, *J. Phys. Chem. C* 114 (13) (2010) 6163–6168, <https://doi.org/10.1021/jp9065949>.
- [46] J. Van De Loosdrecht, S. Barradas, E.A. Caricato, N.G. Ngwenya, P.S. Nkwanyana, M.A.S. Rawat, B.H. Sigwebele, P.J. Van Berge, J.L. Visagie, Calcination of Co-based Fischer-Tropsch synthesis catalysts, *Top. Catal.* 26 (1–4) (2003) 121–127, <https://doi.org/10.1023/B:TOCA.0000012992.97670.0a>.
- [47] E.K. Poels, J.G. Dekker, W.A. Van Leeuwen, Hydrothermal sintering of the active phase in alumina supported fixed bed nickel catalysts during reduction, *Stud. Surf. Sci. Catal.* 63 (C) (1991) 205–214, [https://doi.org/10.1016/S0167-2991\(08\)64586-3](https://doi.org/10.1016/S0167-2991(08)64586-3).
- [48] T.M. Eggenhuisen, P.E. De Jongh, K.P. De Jong, Fundamentals of melt infiltration for supported catalyst preparation. the case of Co/SiO₂ Fischer Tropsch catalysts, *AIChE Annu. Meet. Conf. Proc.* (2010) 18318–18325, <https://doi.org/10.1016/j.cattod.2010.02.052>, 41.
- [49] E.A. Cochran, K.N. Woods, D.W. Johnson, C.J. Page, S.W. Boettcher, Unique chemistries of metal-nitrate precursors to form metal-oxide thin films from solution: materials for electronic and energy applications, *J. Mater. Chem. A* 7 (42) (2019) 24124–24149, <https://doi.org/10.1039/c9ta07727h>.
- [50] P. Melnikov, V.A. Nascimento, I.V. Arkhangelsky, L.Z. Zanonli Consolo, L.C.S. De Oliveira, Thermal decomposition mechanism of iron(III) nitrate and characterization of intermediate products by the technique of computerized modeling, *J. Therm. Anal. Calorim.* 115 (1) (2014) 145–151, <https://doi.org/10.1007/s10973-013-3339-1>.
- [51] P.K. Gallagher, D.W. Johnson, Kinetics of the thermal decomposition of aqueous manganese(II) nitrate solutions on porous tantalum, *J. Electrochem. Soc.* 118 (9) (1971) 1530, <https://doi.org/10.1149/1.2408371>.
- [52] B. Malecka, A. Łącz, E. Drozd, A. Malecki, Thermal decomposition of D-Metal nitrates supported on alumina, *J. Therm. Anal. Calorim.* 119 (2) (2015) 1053–1061, <https://doi.org/10.1007/s10973-014-4262-9>.
- [53] P.K. Gallagher, F. Schrey, B. Prescott, The Thermal decomposition of aqueous manganese (II) nitrate solution, *Thermochim. Acta* 2 (5) (1971) 405–412, [https://doi.org/10.1016/0040-6031\(71\)85016-5](https://doi.org/10.1016/0040-6031(71)85016-5).
- [54] Y. Li, B. Liu, H. Wang, X. Su, L. Gao, F. Zhou, G. Duan, Co₃O₄ nanosheet-built hollow dodecahedrons via a two-step self-templated method and their multifunctional applications, *Sci. China Mater.* 61 (12) (2018) 1575–1586, <https://doi.org/10.1007/s40843-018-9254-6>.
- [55] C. Alex, S.C. Sarma, S.C. Peter, N.S. John, Competing Effect of Co³⁺ reducibility and oxygen-deficient defects toward high oxygen evolution activity in Co₃O₄ systems in alkaline medium, *ACS Appl. Energy Mater.* 3 (6) (2020) 5439–5447, <https://doi.org/10.1021/acsaem.0c00297>.
- [56] S. Yao, H. Wei, Y. Zhang, X. Zhang, Y. Wang, J. Liu, H.H. Tan, T. Xie, Y. Wu, Controlled growth of porous oxygen-deficient NiCo₂O₄ nanobelts as high-efficiency electrocatalysts for oxygen evolution reaction, *Catal. Sci. Technol.* 11 (1) (2021) 264–271, <https://doi.org/10.1039/d0cy01669a>.
- [57] N.-I. Kim, Y.J. Sa, S.-H. Cho, I. So, K. Kwon, S.H. Joo, J.-Y. Park, Enhancing activity and stability of cobalt oxide electrocatalysts for the oxygen evolution reaction via transition metal doping, *J. Electrochem. Soc.* 163 (11) (2016) F3020–F3028, <https://doi.org/10.1149/2.003161jjes>.
- [58] S. Osswald, V.N. Mochalin, M. Havel, G. Yushin, Y. Gogotsi, Phonon confinement effects in the raman spectrum of nanodiamond, *Phys. Rev. B - Condens. Matter Mater. Phys.* 80 (7) (2009) 075419, <https://doi.org/10.1103/PhysRevB.80.075419>.
- [59] C.V. Cushman, P. Brüner, J. Zakeš, G.H. Major, B.M. Lunt, N.J. Smith, T. Grehl, M. R. Linford, Low Energy Ion Scattering (LEIS). A practical introduction to its theory, instrumentation, and applications, *Anal. Methods* 8 (17) (2016) 3419–3439, <https://doi.org/10.1039/c6ay00765a>.
- [60] M.R. Anantharaman, S. Reijne, J.P. Jacobs, H.H. Brongersma, R.H.H. Smits, K. Seshan, Preferential exposure of certain crystallographic planes on the surface of spinel ferrites: a study by leis on polycrystalline spinel ferrite surfaces, *J. Mater. Sci.* 34 (17) (1999) 4279–4283, <https://doi.org/10.1023/A:1004615222119>.
- [61] I. Spolveri, A. Atrei, B. Cortigiani, U. Bardi, A. Santucci, D. Ghisletti, Surface composition of the phases formed by solid state reaction at the Cr/ZnO(0001) interface studied by low energy ion scattering and X-Ray photoelectron spectroscopy, *Surf. Sci.* 412–413 (1998) 631–638, [https://doi.org/10.1016/S0039-6028\(98\)00497-X](https://doi.org/10.1016/S0039-6028(98)00497-X).
- [62] B. Zhang, L. Wang, Z. Cao, S.M. Kozlov, F.P. García de Arquer, C.T. Dinh, J. Li, Z. Wang, X. Zheng, L. Zhang, Y. Wen, O. Voznyy, R. Comin, P. De Luna, T. Regier, W. Bi, E.E. Alp, C.W. Pao, L. Zheng, Y. Hu, Y. Ji, Y. Li, Y. Zhang, L. Cavallo, H. Peng, E.H. Sargent, High-Valence metals improve oxygen evolution reaction performance by modulating 3d metal oxidation cycle energetics, *Nat. Catal.* 3 (12) (2020) 985–992, <https://doi.org/10.1038/s41429-020-00525-6>.
- [63] X. Deng, W.N. Schmidt, H. Tüysüz, Impacts of geometry, symmetry, and morphology of nanocast Co₃O₄ on its catalytic activity for water oxidation, *Chem. Mater.* 26 (21) (2014) 6127–6134, <https://doi.org/10.1021/cm502316g>.
- [64] S. Anantharaj, S.R. Ede, K. Sakthikumar, K. Karthick, S. Mishra, S. Kundu, Recent trends and perspectives in electrochemical water splitting with an emphasis on sulfide, selenide, and phosphide catalysts of Fe Co, and Ni: a review, *ACS Catal.* 6 (12) (2016) 8069–8097, <https://doi.org/10.1021/acscatal.6b02479>.
- [65] J. Wang, R. Gao, D. Zhou, Z. Chen, Z. Wu, G. Schumacher, Z. Hu, X. Liu, Boosting the electrocatalytic activity of Co₃O₄ nanosheets for a Li-O₂ battery through modulating inner oxygen vacancy and exterior Co³⁺/Co²⁺ Ratio, *ACS Catal.* 7 (10) (2017) 6533–6541, <https://doi.org/10.1021/acscatal.7b02313>.
- [66] K. Song, E. Cho, Y.M. Kang, Morphology and active-site engineering for stable round-trip efficiency Li-O₂ batteries: a search for the most active catalytic site in Co₃O₄, *ACS Catal.* 5 (9) (2015) 5116–5122, <https://doi.org/10.1021/acscatal.5b01196>.
- [67] H.Y. Wang, S.F. Hung, H.Y. Chen, T.S. Chan, H.M. Chen, B. Liu, In Operando identification of geometrical-site-dependent water oxidation activity of spinel Co₃O₄, *J. Am. Chem. Soc.* 138 (1) (2016) 36–39, <https://doi.org/10.1021/jacs.5b10525>.
- [68] W. Kang, R. Wei, H. Yin, D. Li, Z. Chen, Q. Huang, P. Zhang, H. Jing, X. Wang, C. Li, Unraveling sequential oxidation kinetics and determining roles of multi-cobalt active sites on Co₃O₄ catalyst for water oxidation, *J. Am. Chem. Soc.* 145 (6) (2023) 3470–3477, <https://doi.org/10.1021/jacs.2c11508>.
- [69] M.S. Burke, M.G. Kast, L. Trotochaud, A.M. Smith, S.W. Boettcher, Cobalt-Iron (Oxy)hydroxide oxygen evolution electrocatalysts: the role of structure and composition on activity, stability, and mechanism, *J. Am. Chem. Soc.* 137 (10) (2015) 3638–3648, <https://doi.org/10.1021/jacs.5b00281>.
- [70] M.S. Burke, S. Zou, L.J. Enman, J.E. Kellon, C.A. Gabor, E. Pledger, S.W. Boettcher, Revised oxygen evolution reaction activity trends for first-row transition-metal (oxy)hydroxides in alkaline media, *J. Phys. Chem. Lett.* 6 (18) (2015) 3737–3742, <https://doi.org/10.1021/acs.jpclett.5b01650>.
- [71] L. Trotochaud, J.K. Ranney, K.N. Williams, S.W. Boettcher, Solution-cast metal oxide thin film electrocatalysts for oxygen evolution, *J. Am. Chem. Soc.* 134 (41) (2012) 17253–17261, <https://doi.org/10.1021/ja307507a>.
- [72] D.A. Corrigan, S.P. Maheswari, Catalysis of the oxygen evolution reaction by trace iron impurities in thin film nickel oxide electrodes, *Electrochem. Soc. Ext. Abstr.* 85–1 (1985) 934–935.
- [73] D.M. Morales, M. Risch, Seven steps to reliable cyclic voltammetry measurements for the determination of double layer capacitance, *JPhysEnergy* 3 (3) (2021), <https://doi.org/10.1088/2515-7655/abec33>.
- [74] L.F. Cueto-Gómez, N.A. García-Gómez, H.A. Mosqueda, E.M. Sánchez, Electrochemical study of TiO₂ modified with silver nanoparticles upon CO₂ reduction, *J. Appl. Electrochem.* 44 (5) (2014) 675–682, <https://doi.org/10.1007/s10800-014-0677-z>.
- [75] M. Chatterjee, S. Sain, A. Roy, S. Das, S.K. Pradhan, Enhanced electrochemical properties of Co₃O₄ with morphological hierarchy for energy storage application: a comparative study with different electrolytes, *J. Phys. Chem. Solids* 2021 (148) (2020) 109733, <https://doi.org/10.1016/j.jpcs.2020.109733>.
- [76] C.I. Priyadharsini, G. Marimuthu, T. Pazhanivel, P.M. Anbarasan, V. Aroulmoji, V. Siva, L. Mohana, Sol-Gel synthesis of Co₃O₄ nanoparticles as an electrode material for supercapacitor applications, *J. Sol-Gel Sci. Technol.* 96 (2) (2020) 416–422, <https://doi.org/10.1007/s10971-020-05393-x>.